

# Control strategies for power enhancement and fatigue damage mitigation of wave cycloidal rotors<sup>★</sup>

Abel Arredondo-Galeana<sup>a,\*</sup>, Andrei Ermakov<sup>b</sup>, Weichao Shi<sup>a</sup>, John V. Ringwood<sup>b</sup> and Feargal Brennan<sup>a</sup>

<sup>a</sup>Department of Naval Architecture, Ocean and Marine Engineering at the University of Strathclyde, Glasgow, UK

<sup>b</sup>Centre for Ocean Energy Research, Maynooth University, Ireland

## ARTICLE INFO

### Keywords:

Wave energy converter  
LiftWEC  
Cyclorotor  
Fatigue analysis  
Velocity control  
Passive pitch

## ABSTRACT

In this paper we perform an analytical and numerical study of the performance of a wave cycloidal rotor in irregular waves, subject to different control strategies. The performance is measured in two ways: Mechanical power, and fatigue damage in a sample stress hot spot located at the fixed end of the hydrofoils. We consider different control strategies seeking to both maximise power extraction and reduce fatigue damage. To maximise power, we consider both constant and variable rotational speed. To mitigate fatigue damage, we consider, for the first time, morphing foils in the context of a wave cycloidal rotor. By testing these control strategies in isolation and in combination, and with the aid of high performance computation, we find that variable rotational speed, in combination with morphing foils, offer the best compromise to enhance power production with a reduced structural penalty on the sample stress hot spot. Hence, in this work, we demonstrate that novel control strategies, such as those proposed in this work, can hold the key in reducing the levelised cost of energy and accelerate the commercialisation of the next generation of lift-based wave energy converters.

**Keywords:** Wave energy converter , LiftWEC, Cyclorotor, Fatigue analysis, Velocity control, Passive pitch

## 1. Introduction

Wave cycloidal rotors are a novel type of wave energy converter (WEC) that have received an increased level of attention over the past decade. Recent efforts in the USA from Atargis [9] and other groups [52], the LiftWEC consortium in Europe [37], and academic efforts in China [13] are driving the momentum in the research of this type of WEC. Wave cycloidal rotors are a particularly enticing WEC due to their control versatility, submerged mode of operation and the potential for reduced levelised cost of energy [28]. Briefly, the device consists of a set of hydrofoils that rotate around a central shaft following the orbital motion of the wave particles, as shown in Figs. 1 and 2. The rotor operates near the water surface but remains submerged with interaction between the foils and waves generating lift forces on the foils, which then sustains the rotation of the device to generate electric power. The use of lift forces, due to the wave hydrofoil interaction, contrasts with more traditional WECs, whose designs exploit buoyancy and/or diffraction forces [14, 16, 35, 48, 54]. At the same time, control technology is reaching a level of maturity for classical

\*This document is the results of the research project funded by the European Union's Horizon 2020 Research and Innovation Programme under Grant Agreement No 851885.

<sup>\*</sup>Corresponding author

✉ abel.arredondo-galeana@strath.ac.uk (A. Arredondo-Galeana); andrei.ermakov@mu.ie (A. Ermakov); weichao.shi@strath.ac.uk (W. Shi); john.ringwood@mu.ie (J.V. Ringwood); feargal.brennan@strath.ac.uk (F. Brennan)  
ORCID(s): 0000-0001-7511-2910 (A. Arredondo-Galeana); 0000-0002-8426-1798 (A. Ermakov); 0000-0001-9730-7313 (W. Shi); 0000-0003-0395-7943 (J.V. Ringwood); 0000-0003-0952-6167 (F. Brennan)

12 WECs [44, 43], including experimental validation [10, 20, 29], while specific control strategies for wave cycloidal  
13 rotors are a topic of current research and development [21, 22, 40].

14 Cyclorotor-based WECs produce unidirectional rotation increasing the efficiency and reducing the cost of power  
15 extraction significantly in comparison with other WECs that typically require rectification of an oscillating motion  
16 [53, 25, 51]. In particular, given that the naturally induced motion is rotational, issues such as the finite stroke  
17 displacement of linear generators do not arise. Furthermore, most traditional WECs are designed to work primarily at  
18 one, or at a limited range of, wave velocities and frequencies with maximum efficiency. In contrast, the reconfigurable  
19 abilities of the hydrofoils of a wave cycloidal rotor can significantly expand the range of useful excitation. For example,  
20 pitch control of the hydrofoils can modulate wave loading on the device, particularly during high power or extreme  
21 wave conditions.

22 However, despite the aforementioned operational advantages, the hydrodynamic and structural complexity of  
23 cyclorotors also makes them vulnerable to fatigue damage and operational breakdown. An example of susceptible  
24 structural points in the cyclorotor are the fixed ends of the hydrofoils, which have been identified to be stress hot spots  
25 [7, 6]. The structural integrity of these hot spots is crucial, since any mechanical failure would likely yield the rotor  
26 inoperational.

27 It is here where the versatility of cyclorotors offers a strategic advantage. Innovative control strategies for hydrofoils,  
28 rotational velocity, and submergence depth could provide power enhancement and, at the same time, avoidance of  
29 significant loads in the foils as well as in the main shaft and support structures. In fact, variable velocity control  
30 of the central shaft has been demonstrated to be a promising technology for cyclorotors to enhance power extraction  
31 [21, 22] in regular waves. However, though some preliminary panchromatic control results are available [21], it remains  
32 unknown whether this strategy is fully applicable in irregular waves and to what extent this type of control impacts the  
33 fatigue damage on the stress hot spots of the foils. Additionally, passive morphing foils are another appealing potential  
34 technological enhancement for cyclorotors. Foils that morph due to fluid forces have shown to reduce loading in cross  
35 flow [5, 8, 31, 32] and tidal turbines [8, 17, 41], but a study on morphing foils remains to be reported in the literature of  
36 cyclorotors. We note that most of these studies represent a morphing foil through a passive pitching mechanism [41],  
37 which is the approach we use in this current study.

38 In this paper, we postulate the hypothesis that, by combining rotational velocity control and passive pitch of the  
39 hydrofoils, we can enhance power extraction while at the same time, we can reduce the structural penalty on the sample  
40 hydrofoil stress hot spot. We investigate our hypothesis through four control cases: 1) Fixed rotational velocity and rigid  
41 foil, 2) variable rotational velocity and rigid foil, 3) fixed rotational velocity and passively pitching foil, and 4) variable  
42 rotational velocity and passively pitching foil.

The remainder of the article is organised as follows: In Section 2, we present an introduction to the operation of wave cycloidal rotors, followed by the concepts of a passive pitching foil and the rotating central shaft in the context of wave cycloidal rotors. In Section 3, we introduce the hydrodynamic model, which accounts for irregular sea states, to reflect realistic sea behaviour. Subsequently, we discuss the fatigue damage methodology. In Section 4, power and fatigue damage results are discussed for the four sample control cases. Lastly, in Section 5, we present our conclusions.

## 2. Operational principle and structural model

### 2.1. Mechanical model of the rotor

The concept of a wave cycloidal rotor is depicted in Figure 1. The figure shows a two foil rotor with symmetric NACA 0015 hydrofoils, as initially proposed within the LiftWEC project [36], operating under the free surface. In this example, the rotor is supported by two tubular triangular frames that are anchored to the sea bed.

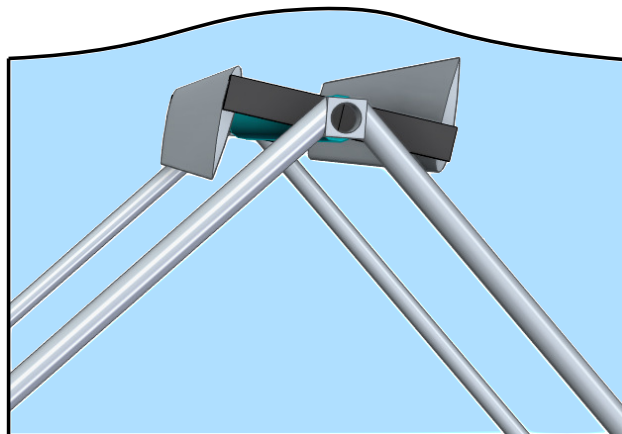


**Figure 1:** Schematic of a wave cycloidal rotor with two hydrofoils rotating under the free surface.

The operation principle of the rotor is summarised in Figure 2. The figure shows a side view of the rotor. The origin of the reference frame  $O(x, y)$  is located above the central shaft and at the mean sea level. The rotor has a submergence  $y_0$  measured from the mean sea level to the central shaft. The radius of the rotor is denoted by  $R$ . The wave propagates from left to right and the wave particle motion is clockwise [12]. The rotation of the hydrofoils follows the circular wave particle motion generating lift  $F_L$  and drag forces  $F_D$ , such that

$$F_L = \frac{1}{2} \rho C S C_L(\alpha) |U|^2 \quad (1)$$

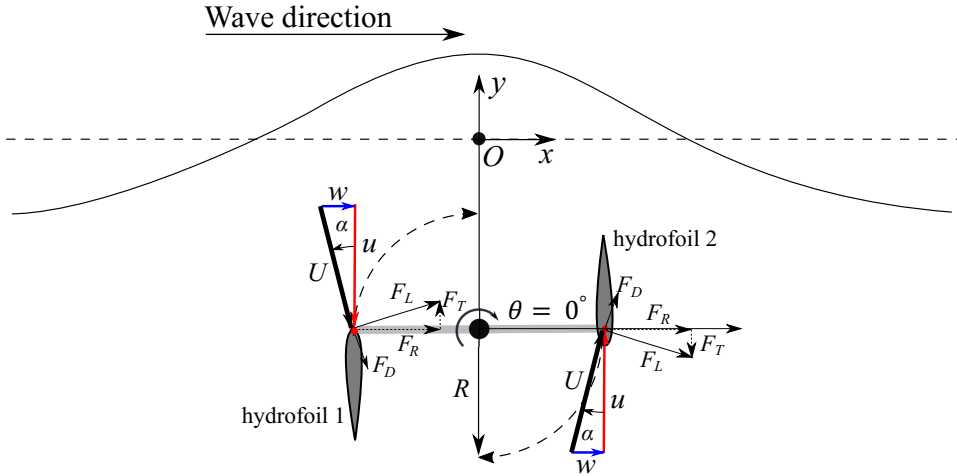


**Figure 2:** Side view of a LiftWEC rotor, showing the lift and drag forces ( $F_L, F_D$ ) on the hydrofoils, the radial and tangential force components ( $F_R, F_T$ ), the wave velocity  $w$ , the velocity due to the rotation of the hydrofoils  $u$ , and the relative fluid velocity to the foil  $U$ . The origin  $O$  of the reference frame is defined at the mean sea level above the central shaft.

59 end

60 
$$F_D = \frac{1}{2} \rho C S C_D(\alpha) |U|^2, \quad (2)$$

61 where  $\rho$  is the fluid density,  $U$  is the relative fluid velocity to the foil,  $S$  is the span of the hydrofoil,  $C$  is the chord  
62 length, and  $C_L(\alpha)$  and  $C_D(\alpha)$  are the lift and drag force coefficients, which are both a function of the angle of attack  $\alpha$ .

63 We note that  $U$  is composed of the vectorial sum of the wave velocity  $w$  and the velocity component due to the rotation  
64 of the foil  $u$ , and that  $\alpha$  is measured between  $u$  and  $U$ , as illustrated in Figure 2. The figure also shows the radial  $F_R$   
65 and tangential forces  $F_T$  acting on the hydrofoils, which are the normal and tangential projections of  $F_L$  and  $F_D$  along  
66 the chord of the hydrofoil.

## 67 2.2. Central shaft dynamics

68 The equation of motion for the central shaft of the wave cycloidal rotor is given by

69 
$$I \ddot{\theta} = \mathcal{T}_{Wave} - \mathcal{T}_{PTO}, \quad (3)$$

70 where  $I$  is the inertia of the rotor,  $\ddot{\theta}$  is the angular acceleration of the rotor,  $\mathcal{T}_{Wave}$  is the hydrodynamic torque and  
71  $\mathcal{T}_{PTO}$  is the control torque of the power take-off (PTO). In Equation (3), the hydrodynamic torque  $\mathcal{T}_{Wave}$  is given by

$$\mathcal{T}_{W\text{ave}} = (F_{T_1} + F_{T_2})R, \quad (4)$$

73 where the indices 1 and 2 refer to hydrofoil 1 and 2, respectively. We recall, from Figure 2, that  $F_T$  is the tangential  
 74 force on the foil and  $R$  is the radius of the rotor.

**75** In Equation (3), the moment of inertia  $I$  is estimated as

$$I = 2mC R^2, \quad (5)$$

where  $m$  is the mass of one of the hydrofoils. Subsequently,  $\mathcal{T}_{PTO}$  can be evaluated from the balance of Equations (3)-(5). In Figure 3, we represent the hydrofoils around the central shaft as a two mass system driven by  $\mathcal{T}_{Wave}$  and  $\mathcal{T}_{PTO}$ , at agreement with Equation (3). It is worth mentioning that, in this stage of design, the mass of the arms that hold the foils, friction due to bearings, and seals in the rotor assembly are not considered in the model of the central shaft dynamics.

82 The performance of the cyclorotor is assessed in terms of the mechanical power generated per second and per span  
83 meter, such that

$$J = \frac{1}{T_0 S} \int_0^{T_0} \mathcal{T}_{PTO}(t) \dot{\theta}(t) dt, \quad (6)$$

where  $\mathcal{T}_{PTO}(t)$  is the instantaneous PTO torque,  $\dot{\theta}(t)$  is the instantaneous rotational velocity of the rotor,  $T_0$  is the duration of the time interval of the power calculation and  $S$  is the span of the hydrofoils. In the following, we define the optimal rotational velocity or optimal frequency, at which  $J$  is maximised as  $\dot{\theta}_0$ .

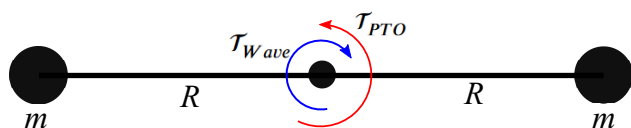


**Figure 3:** Two mass system representing the dynamics of the central shaft, where  $m$  is the mass of the hydrofoil,  $R$  is the radius,  $\mathcal{T}_{W\text{ave}}$  is the hydrodynamic input torque and  $\mathcal{T}_{PTO}$  is the control torque.

### 88 2.3. Morphing foil model

89 Morphing foils, modelled as passively pitching systems, have shown to be a promising technology for peak loading  
 90 alleviation in tidal turbines [8, 17, 41, 49]. However, to date, passive compliance has not been studied for wave energy  
 91 devices and, in particular, for wave energy cyclorotors. In this article, we develop a novel model for passive pitching  
 92 in wave cycloidal rotors, based on the work performed for tidal turbines by Pisetta et al. [41]. We refer to their model  
 93 as the single spring model and present first a brief summary as follows.

94 The single spring model represents a morphing foil by simulating compliance through a torsional spring attached to  
 95 the pitching axis of the foil [41]. The initial equilibrium position is shown in Figure 4a. The pitching axis is located near  
 96 the leading edge of the foil and the distance from the pitching axis to the quarter chord is denoted as  $C_0$ . The torsional  
 97 spring, which is located at the pitching axis, is pretensioned and its torsional moment ( $M_0$ ) opposes and balances the  
 98 mean hydrodynamic moment of the foil ( $\overline{M_H}$ ). Because  $M_0$  and  $\overline{M_H}$  are opposite and equal to each other, a nonzero  
 99 mean angle of attack  $\bar{\alpha}$  can be sustained in the foil, as depicted in Figure 4a. In the figure, where the mean inflow  
 100 velocity is  $\overline{U}$ .

101 Subsequently, during operation, the foil pitches around its pitching axis in the presence of periodic inflow  
 102 oscillations and around  $\bar{\alpha}$ . This scenario is illustrated in Figure 4b. Even though the foil pitches, the spring moment  $M_0$   
 103 is considered constant because the spring is of very low stiffness. The change in the inflow is  $\delta\alpha$ , the change in  $M_H$  is  
 104  $\delta M_H$ , and the change in  $F_R$  is  $\delta F_R$ . Because the pitching axis is upstream of the quarter chord of the foil, the pitching  
 105 motion opposes  $\delta\alpha$ . Hence, the angle of attack on the foil  $\alpha$  and peak loading are attenuated. Because  $\bar{\alpha}$  is maintained,  
 106 mean power production remains unaltered. We note that, in Figure 4b,  $U$  is the new inflow velocity acting on the foil,  
 107  $\phi$  is the pitching angle of the foil and  $\alpha$  is the new angle of attack on the foil after the pitching motion.

108 In a wave cycloidal rotor, the single spring model could work for regular sea state operation. This is because the  
 109 angle of attack of the foil oscillates around a nonzero mean angle of attack [7]. However, for an irregular sea state, the  
 110 mean angle of attack on the hydrofoils is zero. Therefore, the mean hydrodynamic moment is also zero and the moment  
 111 provided by a single pretensioned spring cannot be balanced. In Figure 5, we illustrate, as an example, the time series  
 112 of  $\alpha$  for one of the hydrofoils of the cyclorotor in an irregular sea state ( $T_p = 6$  s and  $H_s = 1$  m). The time series shows  
 113 that the mean angle of attack in the hydrofoil of the cyclorotor is  $0^\circ$ . Note that the computation of  $\alpha$  is performed with  
 114 the hydrodynamic model, which is introduced later in §3.

115 Secondly, in the single spring model, developed for tidal turbines, the hydrodynamic moment coefficient is  
 116 linearised, due to the assumption of small changes in the angle of attack. This assumption does not apply to the case of  
 117 a cyclorotor foil in panchromatic waves [21]. As a result, the hydrodynamic moment coefficient cannot be linearised  
 118 but, instead, its exact value needs to be computed.

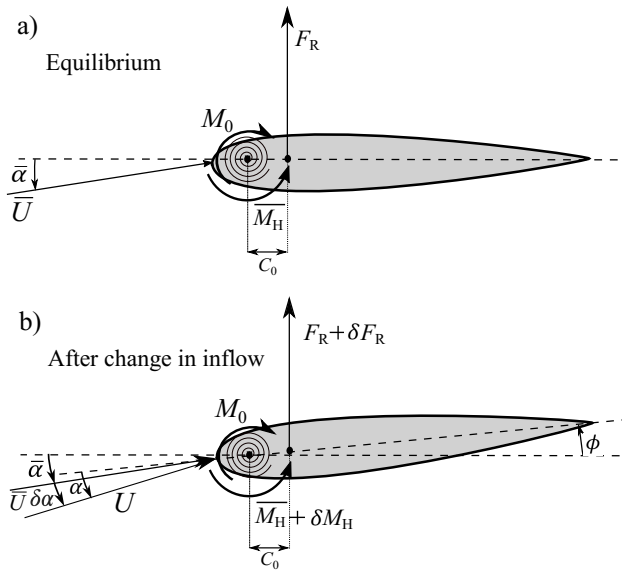


**Figure 4:** Single spring model from Pisetta et al. [41] showing a) the equilibrium position of the morphing foil, modelled with the single spring model with a non zero mean angle of attack  $\bar{\alpha}$  and a mean inflow  $U$ , and b) the new equilibrium position after a change in the inflow and after the foil pitches by an angle  $\phi$ .

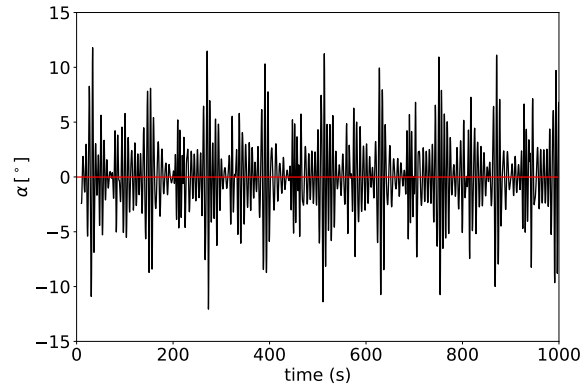


**Figure 5:** Angle of attack oscillations in one of the foils in an irregular sea state ( $T_p = 6$  s,  $H_s = 1$  m). The horizontal red line shows the mean angle of attack.

119 Lastly, the assumption of a very low stiffness spring would yield a hydrofoil that is very sensitive to inflow changes  
 120 and therefore, in a cyclorotor subject to irregular waves, the system could become unstable. As such, we consider a  
 121 stiffness that will allow the foil to pitch, but that still poses some resistance to deformation. This could represent, for  
 122 example, the deformation of a flap near the trailing edge of a foil [8].

123 Therefore, here, we develop a model to represent a passively pitching foil that morphs in the context of a cyclorotor.  
 124 The model compensates for the lack of a nonzero mean hydrodynamic moment by the addition of a second torsional  
 125 spring at the pitching axis. We refer to the model as the dual spring model. The equilibrium position of the foil of the

126 cyclorotor is depicted in Figure 6. The foil is at rest and free to pitch around the pitching axis. The pitching axis is  
 127 located at a distance  $C_p = 0.1C$  from the leading edge. The equilibrium position is enforced with two pretensioned  
 128 springs that oppose each other around the pitching axis. The moments are denoted as  $M_{0,1}$  and  $M_{0,2}$ . Because both  
 129 moments are greater than the weight of the foil and than the buoyancy force, the foil remains at a zero angle of attack  
 130 in equilibrium.

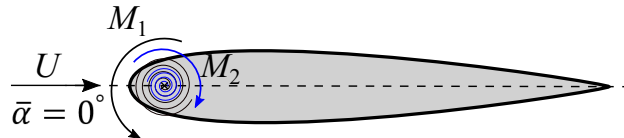


**Figure 6:** The equilibrium position of a morphing foil modelled with the dual spring model for a wave cycloidal rotor operating in irregular waves, where the mean angle of attack is  $\alpha = 0^\circ$ .

131 When the rotor spins in the presence of waves, an instantaneous change in the hydrodynamic moment  $\delta M_H$  will  
 132 occur due to a change in the inflow angle of attack and a new equilibrium position is reached. We depict this scenario  
 133 in Figure 7. In Figure 7, the change in the inflow angle is defined as  $\beta$ , and is measured from the line tangent to the  
 134 circumferential path of the rotor to the direction of the inflow angle  $U$ . Subsequently, because of the change in the  
 135 direction of  $U$ ,  $\delta M_H$  pitches the foil up and a displacement from the neutral position occurs. Because the springs  
 136 are of low stiffness, but rigid enough to oppose a resistance to the pitching motion, the displacement from the neutral  
 137 position causes a change in the torsional moment of each spring  $\delta M_0$ . We show the torsional moments of each spring  
 138  $\delta M_{0,1}$  and  $\delta M_{0,2}$  due to tension and compression, respectively, in the inset of Figure 7. Both of these moments oppose  
 139  $\delta M_H$ . As such, the new equilibrium position will be achieved when

$$140 \quad 2\delta M_0 = \delta M_H. \quad (7)$$

141 In Equation (7)

$$142 \quad \delta M_0 = \kappa \phi, \quad (8)$$

143 where  $\kappa$  is the stiffness of the spring and  $\phi$  is the pitching angle of the foil. In Equation (7), the change in the  
 144 hydrodynamic moment  $\delta M_H$  is defined as

145

$$\delta M_H = \frac{1}{2} \rho C_M C^2 S |U|^2, \quad (9)$$

146 where  $C_M$  is the hydrodynamic pitching moment coefficient,  $\rho$  is the density of the fluid,  $U$  is the relative fluid velocity,  
 147  $S$  is the span of the foil and  $C$  is the chord length. In Equation (9),  $C_M$  is obtained by translating the quarter chord  
 148 hydrodynamic pitching moment  $C_{M,\frac{1}{4}}$  to the pitching axis of the hydrofoil, such that

149

$$C_M = C_{M,\frac{1}{4}}(\alpha) + C_0 [C_L(\alpha) \cos(\alpha) + C_D(\alpha) \sin(\alpha)], \quad (10)$$

150 where  $C_0$  is the distance from the quarter chord position to the pitching axis. We note that the pitching axis is located  
 151 at a distance of  $C_p = 0.1C$  from the leading edge; therefore,  $C_0 = 0.15C$ . We recall that, for symmetric foils, such as  
 152 those used in this cyclorotor,  $C_{M,\frac{1}{4}}(\alpha) = 0$  [1].

153 Substituting relations (8), (9) and (10) into the moment balance given by Equation (7), we obtain a nonlinear  
 154 equation which is solved for  $\phi$ , such that

155

$$\kappa\phi = \frac{1}{4}\rho(C_0[C_L(\alpha)\cos(\alpha) + C_D(\alpha)\sin(\alpha)])C^2S|U|^2 \quad (11)$$

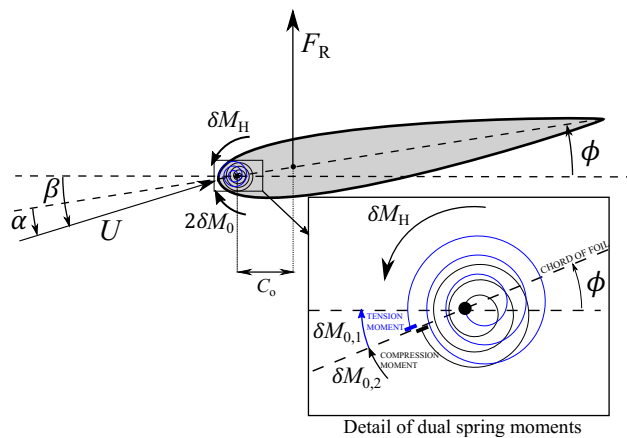


**Figure 7:** a) The new equilibrium position of the morphing foil modelled with the dual spring model after a small change in inflow angle and b) after a large change in inflow angle.

156

where

157

$$\alpha = \beta - \phi. \quad (12)$$

158

In Equation (12),  $\beta$  is the angle between the tangent to the circular trajectory of the foil and the relative fluid velocity  $U$ , as indicated in Figure 7. For a rigid foil that does not pitch,  $\beta = \alpha$ . In contrast, when the foil pitches by  $\phi$ , Figure 7 shows that  $\alpha$ , which is measured between the chord line and  $U$ , decreases. Therefore, the radial force  $F_R$  on the foil should also decrease.

162

Although a well tuned dual spring model reduces  $\alpha$  and the change in the hydrofoil loading, a very low stiffness could come at a price. If the stiffness is too low, then  $\beta = \phi$  and, therefore,  $\alpha = 0^\circ$ . We depict this scenario in Figure 8. As such, the ideal stiffness of the springs is one that reduces  $\alpha$ , but does not nullify it. Hence, a spring system of intermediate stiffness could represent the behaviour of a realistic morphing structure where the deformation is concentrated towards the trailing edge of the hydrofoil.

166

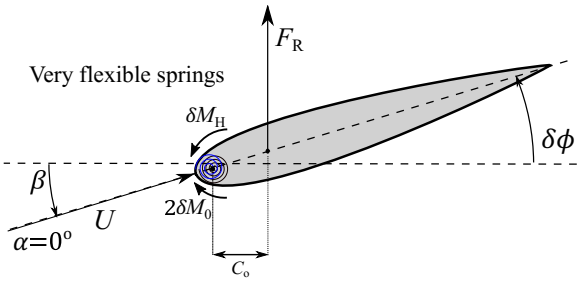


**Figure 8:** The new equilibrium position of the morphing foil modelled with the dual spring model with very flexible springs.

167

## 2.4. Fatigue damage assessment

168

The methodology to compute the fatigue damage on the sample stress hot spot of the cyclorotor is presented in this section. The fatigue damage on a stress hot spot due to an  $i$ -th sea state can be determined through Miner's rule [19, 11], such that

171

$$D_i = \sum_{j=1}^b \frac{365 \times 24 \times P_i}{t} \frac{n_j}{N_j} \frac{1}{S}. \quad (13)$$

172

In Equation (13), we define  $D_i$  as the accumulated fatigue damage per span metre for the  $i$ -th sea state,  $P_i$  is the probability of occurrence of the  $i$ -th sea state,  $t$  is the duration of the stresses time series in the hot spot,  $n_j$  is the

number of cycles at stress range  $\Delta\bar{\sigma}_j$ ,  $N_j$  is the number of cycles to failure at stress range  $\Delta\bar{\sigma}_j$ ,  $b$  is the total number of stress blocks, and  $S$  is the span of the foil.

In Equation (13), the probability  $P_i$  of the  $i$ -th sea state is obtained from the wave climate from the HOMERE database from Ifremer [2]. The data is shown in Figure 9 and corresponds to a point located at  $47.84^\circ$  N,  $4.83^\circ$  W on the North Atlantic coast of France. Each sea state in the database has a duration of 1 hour and the data extends for a period between 2001 and 2010. Note that the database provides the energy period  $T_e$ , rather than the peak period  $T_p$ . For our hydrodynamic model, the conversion between  $T_e$  and  $T_p$  is performed through  $T_e = \lambda T_p$  [3]. Hence, by considering a JONSWAP spectrum of shape factor 3.3,  $\lambda = 0.9$  [15].

Since the data presented in Figure 9 contains 120 sea states and 78879 events, equivalent to 9 years of sea data, to perform our damage computations, we downsampled the grid from 120 sea states to 30 sea states over the range of  $6 \text{ s} \leq T_p \leq 16 \text{ s}$  and  $1 \text{ m} \leq H_s \leq 5 \text{ m}$ , in steps of 2 s and 1 m, respectively. This window of sea states accounts for a total probability of occurrence of 98%. As such, the  $P_i$  values of Figure 9 are grouped in representative clusters around a reduced grid of 30 sea states. Subsequently, the computed values of damage are interpolated to a finer grid of  $21T_p$  and  $25H_s$  to present our results. The same interpolation procedure is also applied to present the  $J$  results.

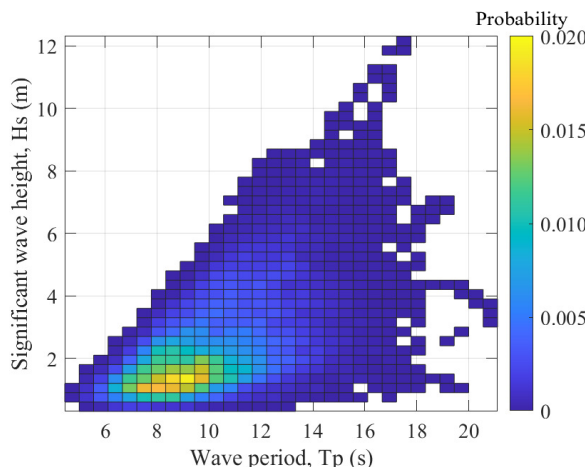


**Figure 9:** Probability data of HOMERE database for a point in the North Atlantic coast of France with  $T_p$  and  $H_s$  in the horizontal and vertical axis, respectively

In Equation 13, the number of cycles to failure  $N$ , for any given  $j$ -th stress range, is obtained from the SN curve of the specific material. The SN curve gives the relationship between the stress range  $\Delta\bar{\sigma}$  and  $N$ , and is given by

$$\log N = \log \bar{a} - \bar{m} \log \Delta\bar{\sigma}, \quad (14)$$

where  $N$  is the number of cycles to failure at stress range  $\Delta\bar{\sigma}$ ,  $\bar{m}$  is the negative inverse slope of the SN curve and  $\log \bar{a}$  is the intercept of the log  $N$  axis by the SN curve. In this work, we use an SN curve of type C for offshore steel in seawater with cathodic protection [19]. This type of curve is recommended for smooth extruded finishes, such as that of the hydrofoils in a cyclorotor. We plot the corresponding SN curve in Figure 10.

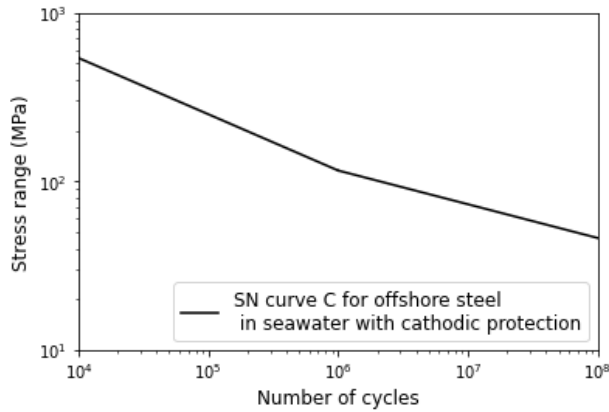


Figure 10: SN curve of type C for offshore steel in seawater with cathodic protection.

Equation (14) can be rewritten in exponential form, such that

$$N = \bar{a} \Delta \bar{\sigma}^{-\bar{m}}, \quad (15)$$

where  $\bar{a}$  and  $\bar{m}$  are properties of the material. We utilise this expression to compute  $N$  for the  $j$ -th stress range in Equation (13).

In this paper,  $\Delta\bar{\sigma}$ , which refers to the stress range measured from peak to trough and vice-versa, is obtained from the time series of the bending stresses  $\bar{\sigma}$  measured at one of the fixed ends of the hydrofoils. These stress hot spots are illustrated in Figure 11. Because the foil is symmetric in the spanwise direction and because we assume two dimensional flow, i.e. large span foils, we consider  $\Delta\bar{\sigma}$  at both hot spots to be equal, and therefore we compute the fatigue damage in one hot spot only.

The stresses on the hotspots are computed following the procedure described in [7, 6]. As part of the procedure, we approximate the cross section of the foil as a square hollow section (SHS) of dimension  $0.15C \times 0.15C$  and a skin thickness of 10 mm. The cross section is shown in the inset of figure 11. The second moment of area  $I_{xx}$  of the cross section depends mainly on the height. As such, the SHS approximation provides a baseline for mechanical design and for the first pass of our fatigue damage analysis. Furthermore, as part of the procedure to compute the bending stresses, the bending moments are computed from the radial forces acting on the foil by assuming that the foil is a fixed beam

210 subject to a uniformly distributed loading. Hence,  $\bar{\sigma}$  at just one of the foil stress hot spots is computed, such that

211

$$\bar{\sigma} = \frac{My_{xx}}{I_{xx}}, \quad (16)$$

212 where  $M$  is the bending moment at the stress hot spot,  $y_{xx}$  is the distance from the symmetric horizontal axis of the  
 213 SHS to the outer shell, and  $I_{xx}$  is the second moment of area of the SHS. Once  $\bar{\sigma}$  is known, then we compute  $\Delta\bar{\sigma}$  from  
 214 the time series of  $\bar{\sigma}$ . Lastly, we use Equation (13) to compute  $D_i$  for the  $i$ -th sea state.

215 **3. Wave-foil interaction model**

216 This section describes the model used to estimate the forces acting on the hydrofoils of the cyclorotor. Each  
 217 hydrofoil is modeled as a point vortex beneath the free surface. The model has been previously developed and applied  
 218 to wave cycloidal rotors in the works of Ermakov and Ringwood [23, 26] under regular waves and has been validated  
 219 for attached flow conditions by Arredondo-Galeana et al. [6]. Here, we provide a summary of the model and implement  
 220 an additional module to consider irregular waves.

221 **3.1. Point-vortex model**

222 The complex potential of a point vortex, under a free surface, was derived by Wehausen and Laitone [50]. This  
 223 representation has been used widely in wave cyclorotor modelling by Hermans [30], Siegel et al. [46] and Ermakov  
 224 and Ringwood [23, 27] to compute the free surface elevation downstream of the rotor and, recently, to estimate the  
 225 loads in the hydrofoils of a cyclorotor under attached flow conditions [7, 26, 6]. In this paper, we utilise this potential  
 226 flow model to compute the forces on the hydrofoils. We then implement different control strategies and assess the  
 227 mechanical power and fatigue damage performance.

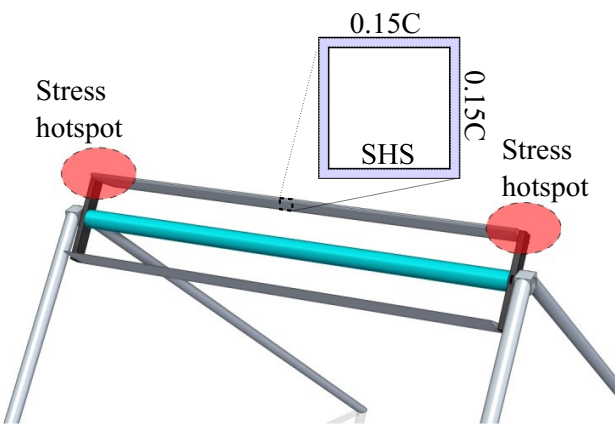


**Figure 11:** Stress hot spots at fixed end of foils in wave cycloidal rotor

228 The point vortex model has been derived in the form of the complex potential in [24] as

$$\begin{aligned} \text{229} \quad F(z, t) &= \frac{\Gamma(t)}{2\pi i} \operatorname{Log} \left[ \frac{z - \zeta}{z - \zeta'} \right] - \\ \text{230} \quad &\frac{2i\sqrt{g}}{\pi} \int_0^t \frac{\Gamma(\tau)}{\sqrt{i(z - \zeta')}} D_w \left[ \frac{\sqrt{g}(t - \tau)}{2\sqrt{i(z - \zeta')}} \right] d\tau, \\ \text{231} \end{aligned} \quad (17)$$

232 where  $z$  is the complex variable,  $t$  is time,  $\zeta$  is the position of the point-vortex,  $\zeta'$  is the complex conjugate of  $\zeta$ ,  $\Gamma$  is the circulation of the point vortex,  $g$  is the gravitational constant,  $k$  is the wave number and  $D_w[x]$  is the Dawson function denoted by:

$$\text{235} \quad D_w[x] = e^{-x^2} \int_0^x e^{y^2} dy. \quad (18)$$

236 The first term of Equation (17) represents the complex potential of a point vortex of circulation  $\Gamma$  under a free surface. The point vortex is located at  $\zeta$ . A mirror vortex is located above the free surface at  $\zeta'$  to impose the impermeability condition. The second term in Equation (17) represents the complex potential of the waves radiated due to the wake of the foil. We note that the second term typically consists of two integrals, one over time  $t$  and another one over the wave number  $k$  [30, 46]. Here, we use the expression derived in Ermakov and Ringwood [24] which solves the integral over  $k$  analytically with the Dawson function. In the integration of Equation (17), the lifetime of the generated wake is considered to be two full rotational periods of the foil.

243 The circulation of the point vortices,  $\Gamma_1$  and  $\Gamma_2$ , is computed from the lift force definition given by Equation (1), and by applying the Kutta condition, we get

$$\text{245} \quad \Gamma = F_L / (\rho |\hat{V}|) = \frac{1}{2} C_L(\alpha) |\hat{V}| C. \quad (19)$$

246 Considering that hydrofoil 1 is located at  $z$ , we can evaluate the influence of hydrofoil 2 and the wakes of both hydrofoils on the velocity field at point  $z$ . Then, the velocity field  $\mathbf{w}_\Gamma$  at point  $z$  is obtained as

$$\text{248} \quad \mathbf{w}_\Gamma = \frac{\partial(F_1(z, t) + F_2(z, t))}{\partial z} = w_{\Gamma x} - iw_{\Gamma y}. \quad (20)$$

249 In Equation (20), the influence of  $\partial F_i(z, t)/\partial z$  on foil  $i$  is only due to the second term of Equation (17). This is  
 250 because when  $\zeta = z$ , the first term of equation (17) has a singularity. However, the further away the wake vortex is  
 251 from the foil, the less influence it exerts on the velocity field of the foil, as specified by Dawson's function in Equation  
 252 (17). The exact terms for the complex velocity of a two foil cyclorotor, which are used in this work, are those found in  
 253 Ermakov and Ringwood [24].

254 Once the velocity field due to the circulation of the foils and their wakes is assessed, we determine the velocity  
 255 components on the foils due to the rotation of the foils and due to the irregular waves. Then, these velocity components  
 256 are combined to determine the relative inflow velocity on the hydrofoil, as well as the angle of attack. Then, we introduce  
 257 the methodology to compute the hydrofoil velocity and the irregular wave velocity components.

### 258 3.2. Hydrofoil velocity

259 The foil velocity components are obtained as follows. Consider a rotor of radius  $R$ , as depicted in Figure 2. The  
 260 position of the hydrofoils, in cartesian coordinates, is given by

$$261 \quad x = R \cos(\theta(t) + \psi) \quad (21)$$

262 and

$$263 \quad y = y_0 - R \sin(\theta(t) + \psi), \quad (22)$$

264 where  $y_0$  is the submergence of the rotor,  $\theta(t)$  is the angular position with respect to the positive horizontal axis and  
 265 positive clockwise, and  $\psi$  is the initial angular position of each hydrofoil, also measured from the positive horizontal  
 266 axis. For the rotor shown in Figure 2,  $\psi = 180^\circ$  for hydrofoil 1 and  $\psi = 0^\circ$  for hydrofoil 2. The rotational velocity  
 267 components  $\mathbf{u} = (u_x, u_y)$  of the hydrofoils are obtained through derivation of equations 21 and 22, such that

$$268 \quad u_x = -\dot{\theta}(t)R \sin(\theta(t) + \psi) \quad (23)$$

269 and

$$270 \quad u_y = -\dot{\theta}(t)R \cos(\theta(t) + \psi), \quad (24)$$

271 where  $\dot{\theta}(t)$  is the rotational velocity of the rotor.

**272 3.3. Irregular wave velocity components**

**273** A JONSWAP wave spectrum is discretised in frequency and used to generate individual waves of wave amplitude  
**274**  $A_j$ , where  $j$ , in this case, is the index denoting the individual wave. The procedure to discretise the spectrum is typically  
**275** used in design studies of different types of WECs [34, 33, 39]. We summarise the procedure as follows. The amplitude  
**276** of the discrete wave components is given by

$$\text{277} \quad A_j = \sqrt{2S_A(\omega_j)\Delta\omega}, \quad (25)$$

**278** where  $S_A(\omega_j)$  is the amplitude of the spectrum at the  $j$ -th frequency  $\omega_j$ , and  $\Delta\omega$  is the discretisation step of the  
**279** spectrum.

**280** We utilise the definition of the JONSWAP spectrum provided by the DNV Environmental Conditions And  
**281** Environmental Loads Practice Manual [18], which states that the JONSWAP spectrum is given by

$$\text{282} \quad S_A(\omega_j) = A_\gamma S_{PM}(\omega_j) \gamma \exp\left[-0.5\left(\frac{\omega_j - \omega_p}{\sigma\omega_p}\right)^2\right], \quad (26)$$

**283** where  $S_{PM}$  is the Pierson-Moskowitz spectrum that is defined as

$$\text{284} \quad S_{PM}(\omega_j) = \frac{5}{16} H_s^2 \omega_p^4 \omega_j^{-5} \exp\left[\frac{-5}{4} \left(\frac{\omega_j}{\omega_p}\right)^{-4}\right] \quad (27)$$

**285** and

$$\text{286} \quad A_\gamma = 1 - 0.287 \ln(\gamma). \quad (28)$$

**287** In Equation (26),  $\omega_p = 2\pi/T_p$ , and  $\sigma = 0.07$  if  $\omega_j \leq \omega_p$ , or  $\sigma = 0.09$  if  $\omega_j > \omega_p$ . Finally,  $\gamma = 3.3$  is the spectrum  
**288** width factor.

**289** The velocity field corresponding to each individual  $j$ -th wave is computed with linear deep water wave theory [4],  
**290** such that

$$\text{291} \quad w_{x,j} = \frac{\pi A_j}{T} e^{k_j y} \cos(k_j x - \omega_j t + \eta_j) \quad (29)$$

**292** and

$$\text{293} \quad w_{y,j} = \frac{\pi A_j}{T} e^{k_j y} \sin(k_j x - \omega_j t + \eta_j), \quad (30)$$

where  $A_j$ ,  $k_j$ ,  $\omega_j$  and  $\eta_j$  are the height, number, angular frequency, and phase of the  $j$ -th wave, respectively,  $x$  and  $y$  are the horizontal and vertical positions of the hydrofoils, as defined by Equations (21) and (22), respectively. Each  $k_j$  is computed with three iterations of the dispersion relationship [38], where the first iteration assumes  $k_j = 1$ . The phase of each discrete wave  $\eta_j$  is randomly assigned within a range of 0 to  $2\pi$  radians.

The total wave induced fluid velocity components  $\mathbf{w} = (w_x, w_y)$  are obtained by adding all  $\omega_{x,j}$  and  $\omega_{y,j}$ , such that

299

$$w_x = \sum_{j=1}^n w_{x,j} \quad \text{and} \quad w_y = \sum_{j=1}^n w_{y,j}. \quad (31)$$

Lastly, the power  $J_w$  available in an irregular wave is defined as

$$J_w = \frac{1}{64\pi} \rho g^2 H_s^2 \lambda T_p. \quad (32)$$

### 3.4. Relative velocity and angle of attack on hydrofoil

The relative velocity  $\mathbf{U}$  acting on the hydrofoil is determined such that

$$\mathbf{U} = \mathbf{w} - \mathbf{u} + \mathbf{w}_{\Gamma_1} + \mathbf{w}_{\Gamma_2}, \quad (33)$$

where  $\mathbf{w}$  is the wave induced fluid velocity,  $\mathbf{u}$  is the rotational velocity of the foil and  $\mathbf{w}_{\Gamma_1}$  and  $\mathbf{w}_{\Gamma_2}$  are the induced velocities due to the waves radiated by the foils. Then, we can compute  $\alpha$  as the angle between  $\mathbf{U}$  and  $\mathbf{u}$ , as defined in Figure 2 and by incorporating the effect of  $\phi$ , as illustrated in Figure 7 for the case of a foil that passively pitches, such that

$$\alpha = \sin^{-1} \left( \frac{|\mathbf{U} \times \mathbf{u}|}{|\mathbf{U}| |\mathbf{u}|} \right) - \phi, \quad (34)$$

where,

$$\beta = \sin^{-1} \left( \frac{|\mathbf{U} \times \mathbf{u}|}{|\mathbf{U}| |\mathbf{u}|} \right), \quad (35)$$

in agreement with Equation (12). Once  $\alpha$  is computed, a NACA 0015 look-up table is utilised to obtain  $C_L$  and  $C_D$  for each hydrofoil. Finally, by defining the chord length  $C$  and the span of the foil  $S$ , and utilising Equations (1) and (2),  $F_L$  and  $F_D$  can be determined. The tangential force in the hydrofoils is defined as

$$_{316} \quad F_T = F_L \sin(\alpha + \phi) - F_D \cos(\alpha + \phi) \quad (36)$$

**317** and the radial force is

$$_{318} \quad F_R = F_L \cos(\alpha + \phi) + F_D \sin(\alpha + \phi). \quad (37)$$

It is worth mentioning that  $F_T$  is tangential and  $F_R$  is normal to the circumferential path of rotation of the cyclrotor.

Therefore, Equations (36) and (37) include the term  $\phi$ .

In Equations (36) and (37),  $F_T$  is responsible for the mechanical power generation, whilst  $F_R$  causes the structural load and fatigue of the foil structure.

## **323 4. Results**

In this section we present the power performance  $J$  and fatigue damage  $D$  at the foil stress hot spot, as defined in Equations (6) and (13), respectively. We present results for four different control strategies: 1) rigid foil and constant rotational velocity, 2) rigid foil and variable rotational velocity, 3) passively pitching foil at constant rotational velocity, and 4) passively pitching foil at variable rotational velocity. We study  $J$  and  $D$  over the range of sea states specified in §2.4.

### **329 Case 1: Rigid foil with constant rotational velocity**

The baseline case consists of a wave cycloidal rotor, with rigid foils, spinning at a constant rotational velocity. We consider a cyclorotor with two hydrofoils. The rotor has a radius of  $R = 6$  m, the hydrofoils have a NACA0015 cross section with chord length  $C = 6$  m, following the design guidelines proposed by the LiftWEC consortium [37]. We note that these design parameters are also similar to those proposed by the Atargis Energy Corporation [47].

To account for inertial effects, we use a cross sectional mass per square metre of  $2\text{kg/m}^2$  for each hydrofoil. For the rotor, we consider adjustable submergence that changes with each sea state, such that  $y_0 = -1.5R - 0.5H_s$ . This promotes efficient power capture by ensuring that the rotor remains in close proximity to the free surface but that the hydrofoils always remain submerged during operation [45].

As a first design step, for each of tested sea states, we match the rotational frequency of the rotor ( $\dot{\theta}$ ) to the peak frequency ( $\omega_p$ ) of a JONSWAP spectrum. We refer to the power under this scenario as  $J_0$ , with results as shown in Figure 12. In the figure, we note that a large portion of the matrix yields  $J_0 < 0 \text{ kW s}^{-1} \text{m}^{-1}$ . Although a pitch angle can

be introduced to the hydrofoils to increase  $J_0$  [47, 6], in this paper, we propose variable velocity control as a mechanism to increase power production. We follow the procedure proposed by Ermakov et al. [21].

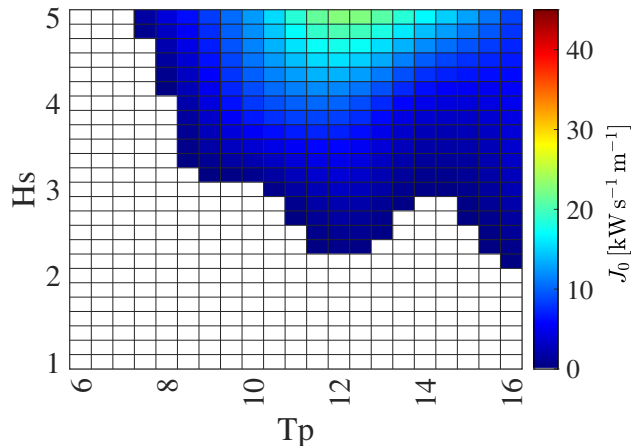


**Figure 12:** Average mechanical power  $J_0$  [ $\text{kW s}^{-1} \text{m}^{-1}$ ] generated when  $\dot{\theta}_0 = \omega_p$ , i.e. without optimisation of rotor rotational rate.

The optimal rotational speed is found with the use of high performance computing facilities from the Irish Centre for High-End Computing (ICHEC) (<https://www.ichec.ie/>) and the ARCHIE-WeST High Performance Computer in Scotland (<https://www.archie-west.ac.uk/>). For each sea state, we conduct trials of 15 minutes averaged over 20 different sea state realisations, to ensure statistically significance of the results. The optimal rotational speed is found by varying the rotational speed of the rotor, in steps of 0.1 rad/s, until the maximum power is encountered. We note that this rotational speed maximises the tangential force on the hydrofoils, and therefore, also the lift-to-drag ratio.

Results for the optimal constant rotational speed  $\dot{\theta}_0$  are presented in Figure 13, normalised by  $\omega_p$ . The figure shows that  $\dot{\theta}_0/\omega_p$  grows from low values ( $0.2 \leq \dot{\theta}_0/\omega_p \leq 0.5$ ) to high values ( $2.5 \leq \dot{\theta}_0/\omega_p \leq 4.0$ ) as  $T_p$  and  $H_s$  increase.

The power output of the rotor running at  $\dot{\theta}_0/\omega_p$  is shown in Figure 14. One realisation per sea state is run for a time period of one hour. Because this is the first control strategy, we denote this power as  $J_1$ . Figure 14 shows that the highest  $J_1$  occurs at the upper right corner of the figure, i.e.  $J_1$  grows with both  $H_s$  and  $T_p$ . A limited area where  $\dot{\theta}_0/\omega_p = 1$  is the only region where the non optimised solution of Figure 12 and the optimised solution of Figure 14 overlap. Note that, the shape of Figure 14 matches the distribution of power available in the irregular waves given by Equation (32). In fact, assuming a zero pitch angle in the foils, efficiencies of up to 0.15 to 0.20 can be achieved, at constant rotational speed.

To understand better the damage footprint on the hydrofoil stress hot spot due to  $P_i$ , we plot, in Figure 15a,  $D_1$  assuming  $P_i = 1$ , while, in Figure 15b, we plot  $D_1$  considering the  $P_i$  shown in Figure 9. We refer to both results as  $D_1(P_i = 1)$  and  $D_1$ , respectively. The duration of these runs are the same as those used to compute  $J_1$ .

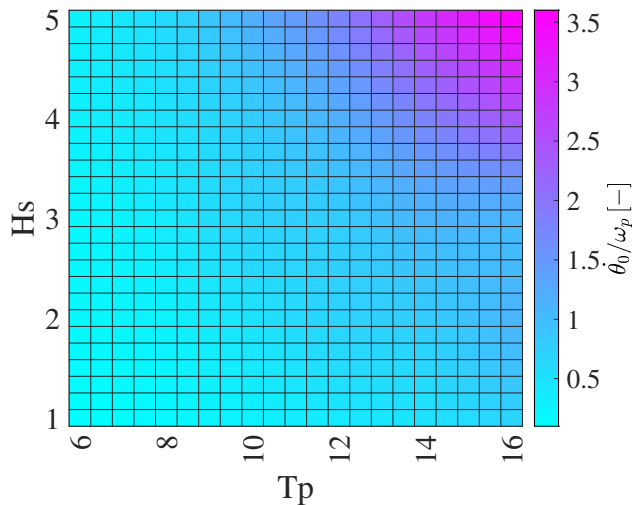


**Figure 13:** Optimal normalised constant rotational rate  $\dot{\theta}_0/\omega_p$  for various panchromatic sea states.

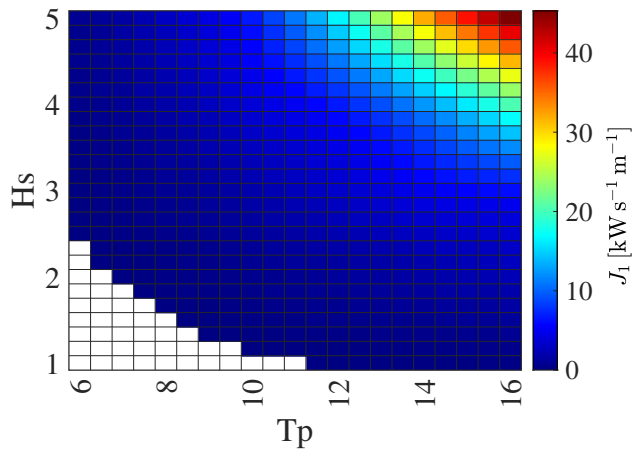


**Figure 14:** Average mechanical power  $J_1$  [ $\text{kW s}^{-1} \text{m}^{-1}$ ] generated with the rotor operating at  $\dot{\theta}_0/\omega_p$ .

361 Figure 15a shows that, the highest  $D_1(P_i = 1)$  occurs at the highest  $H_s$  and the lowest  $T_p$ . This is in contrast to the  
 362 location of the highest peak in  $J_1$ , and therefore contradicts what is typically expected, which is that the location of  
 363 the peak in damage is usually the same location as the peak in power. However, in the case of the sample stress hot  
 364 spot analysed in this study, although the peak of both  $J_1$  and  $D_1(P_i = 1)$  occur at the highest  $H_s$ , the rotor spins faster  
 365 at low  $T_p$ . Hence, more loading cycles occur at the lowest  $T_p$  values and therefore more damage occurs, as shown in  
 366 Figure 15a.

367 Then, the effect of  $P_i$  in  $D_1$  is shown in Figure 15b. The location of the highest peak in  $D_1$  is shifted towards  
 368 intermediate  $T_p$  values, but consistently at  $H_s = 5$  m. Noticeably, a secondary peak appears at  $H_s \approx 3$  m and  $T_s \approx 8$  s.  
 369 The shift in position of the highest peak in  $D_1$  is a result of the distribution of  $P_i$  at  $H = 5$  m, with the highest  $P_i$  at

370 intermediate  $T_p$  values. The secondary peak in  $D_1$  is a result of the combined effect of sea states with high probability  
 371 of occurrence ( $P_i \geq 0.14$ ) and a high number of cycles, due to the fast rotation of the cyclorotor at low  $T_p$ . Assuming a  
 372 span of  $S = 10$  m, and offshore steel with cathodic protection, Figure 15b yields a yearly cumulative fatigue damage  
 373 of  $D_1 = 0.004$ . This is equivalent to 25 years of useful lifetime of the hydrofoil, before mechanical failure.

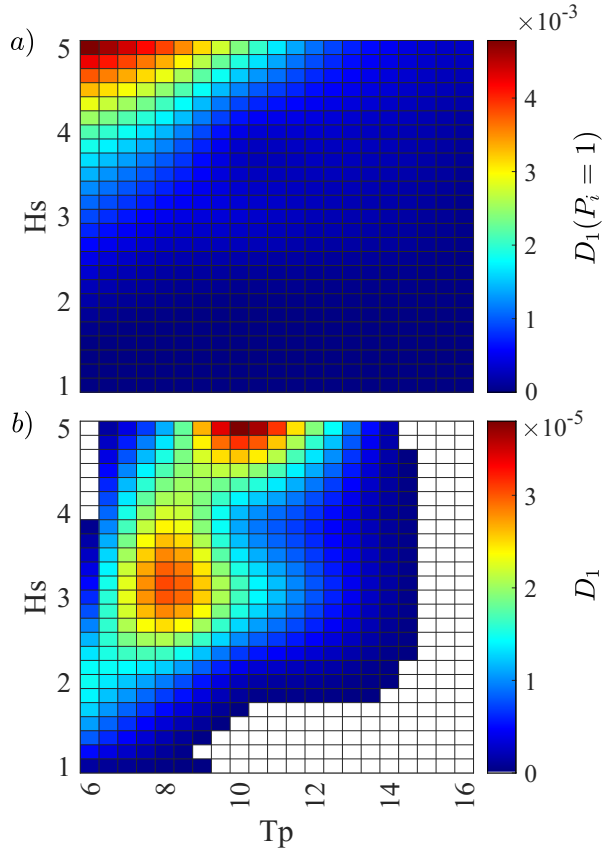


**Figure 15:** Yearly damage  $D_1$  at the foil hot spot, generated with  $\dot{\theta}_0/\omega_p$  when a)  $P_i = 1$  and b) when  $P_i$  is that of Figure 9.

374 **Case 2: Rigid foil with variable rotational velocity**

375 We now consider the influence of variable rotational velocity on  $J$  and  $D$ . For Case 2, we refer to these as  $J_2$  and  
 376  $D_2$ , respectively. Previous research has shown that variable velocity control can increase the mechanical power by up  
 377 to 40% [21, 22] in monochromatic and also in panchromatic waves. However, the effect of this control strategy, for  
 378 a wide range of irregular sea states, remains unknown, as well as the impact in the radial loading and the structural  
 379 penalty at the hydrofoil sample hot spot. Therefore, we investigate these aspects in this section.

380 We note that, in Case 2, the control of the instantaneous rotational velocity has the objective of maximising  $J_2$ .  
 381 We recall that  $J_2$  is a function of the rotational velocity  $\dot{\theta}(t)$ , as defined by Equation (6). Therefore, by considering  $\dot{\theta}_0$   
 382 from the baseline case, we can add a series of harmonics to  $\dot{\theta}_0$  and find the time dependent solution that maximises  $J_2$ .

383 Specifically, we apply a spectral method [42], which finds the solution of an equation through a sum of basis functions,  
 384 in this case a Fourier series. With such a choice,  $\theta(t)$  is expressed as

$$385 \quad \theta(t) = \dot{\theta}_0 t + \sum_{i=1}^h a_i \cos\left(\frac{2\pi}{T_{ext}} i + c_i\right) + \\ 386 \quad b_i \sin\left(\frac{2\pi}{T_{ext}} i + d_i\right), \quad (38)$$

387 where  $\theta(t)$  is the angular position of the rotor,  $\dot{\theta}_0$  is the constant optimal rotational velocity found in Case 1,  $t$  is time,  
 388  $a_i$  and  $b_i$  are the Fourier coefficients,  $c_i$  and  $d_i$  are phase shifts to the harmonic terms of the Fourier series, and  $h$  is the  
 389 total number of harmonics used in the solution. By combining the first derivative of Equation (38) with Equation (6),  
 390 we obtain the solution of  $\dot{\theta}(t)$  that maximises  $J_2$ .

391 The coupled system of equations ((6) and (38)) is solved for an extended time period  $T_{ext} = 3T_0$ , where  $T_0$  is the  
 392 power production period. We note that  $J_2$  is extracted from  $T_0 < t \leq 2T_0$ , to eliminate initial and final transients.  
 393 The maximum  $J_2$  and the Fourier coefficients  $a_i$ ,  $b_i$ ,  $c_i$  and  $d_i$ , for every harmonic  $i$ , are found in Python using the  
 394 "minimize" function of the "optimize" package. As part of the optimisation algorithm, the ratio  $\dot{\theta}/\dot{\theta}_0$  is constrained to  
 395  $1/2 < \dot{\theta}/\dot{\theta}_0 < 2$ , where  $\dot{\theta}$  is the rotational speed specified in Equation (6). The convergence of the method with these  
 396 constraints is shown in [21, 22].

397 It is worth mentioning that the optimisation of the performance function (Eq. (6)) requires the solution of a highly  
 398 nonlinear problem [23]. In order to achieve acceptable convergence of the developed spectral method (Eq. (38)), it  
 399 was decided to limit the simulation to one minute only. This involved the use of at least 25 harmonics, each with  
 400 four different  $a_i$ ,  $b_i$ ,  $c_i$  and  $d_i$  coefficients, to find the solution to the problem. For every sea state, the average power  
 401 performance  $J_2/J'_1$ , and the average fatigue damage performance  $D_2/D'_1$ , are computed by adding the corresponding  
 402  $J_2$ ,  $J'_1$ ,  $D_2$  and  $D'_1$  for each of the simulations, and by calculating their ratio. The same procedure to compute the  
 403 average power performance and fatigue performance is repeated in Case 3 and Case 4.

404 Results for Case 2 are presented in Figures 16a and 16b, respectively. Figure 16a shows the  $J_2/J'_1$  ratio. The figure  
 405 shows that the ratio remains between  $1.5 \leq J_2/J'_1 \leq 2.5$ . These results represent gains of about 50% to 150% percent  
 406 with respect to the case of constant rotational velocity. It is noted that Figure 16a has a similar shape to the power  
 407 matrix computed with real-time velocity control in monochromatic waves, as presented in Ermakov et al. [21]. This  
 408 shows that similar power performance can be expected between regular and irregular sea states.

409 Figure 16b shows the  $D_2/D'_1$  ratio. It can be seen that  $D_2$  is about 10 times higher than  $D'_1$ . However, at the top  
 410 left side of the figure, where low  $T_p$  and high  $H_s$  occur,  $D_2$  is about 80 times higher than  $D'_1$ . This shows that the gain  
 411 in power comes at the cost of an increase in fatigue damage at the foil hot spot and that, in fact, the increase in damage

is significantly higher than the increase in power output. For instance, if we consider that, in general,  $D_2/D'_1 \approx 10$ , variable rotational speed could reduce the lifetime of a 10 m span wave cycloidal rotor from 25 to 2.5 years.

#### **414 Case 3: Passively pitching foil with constant rotational velocity**

415 Case 3 evaluates the effect of morphing foils, modelled as passively pitching foils, on the performance of wave  
 416 cycloidal rotors. Similarly to what has been shown in tidal turbines, it is expected that the radial load on the hydrofoil  
 417 is reduced and consequently, that the bending stresses and fatigue damage are reduced as well. However, because this  
 418 is the first time that such concept is evaluated in the context of a wave cycloidal rotor, it is unknown to what extent this  
 419 control strategy can influence the power output.

420 We recall that the single spring model developed for tidal turbines [41] was developed assuming a nonzero mean  
 421 angle of attack and periodic oscillations. Hence, such a model is not suitable to represent a morphing hydrofoil in the  
 422 context of a wave cycloidal rotor, especially and under the influence of irregular waves. Therefore, we compensate  
 423 the lack of a nonzero mean angle of attack, and a nonzero mean hydrostatic moment, by incorporating another spring

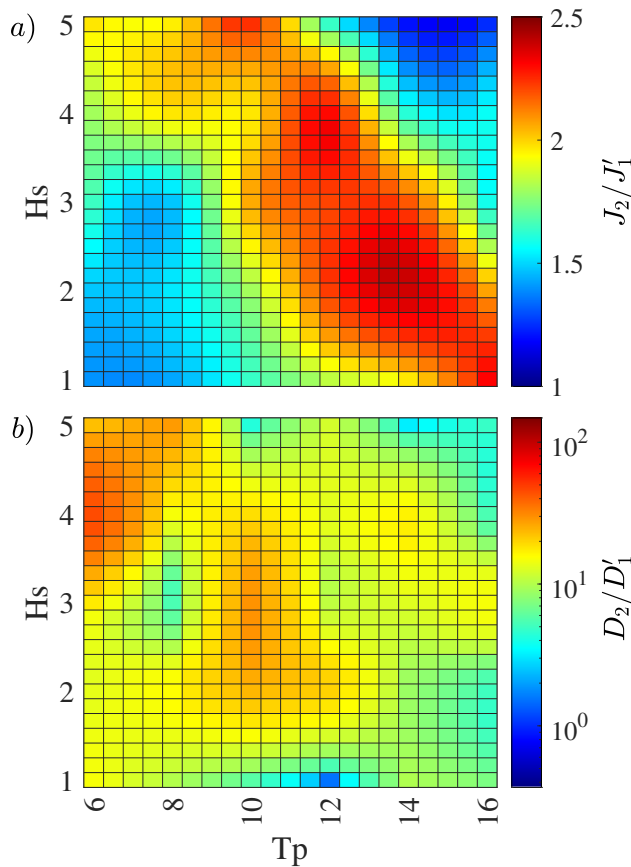


**Figure 16:** a)  $J_2/J'_1$  ratio and b)  $D_2/D'_1$  ratio with variable time-dependent rotational velocity.

424 in the model. The second spring allows the hydrofoils of the cyclorotor to sustain the equilibrium position shown in  
 425 Figure 6.

426 We first assess the performance of the dual spring model in a regular wave scenario, where the rotor has a phase  
 427 shift of  $-90^\circ$  with respect to the wave crest [7, 23]. In regular waves, the rotor operates typically at a rotational velocity  
 428 equivalent to the wave frequency  $\dot{\theta} = \omega$ . We consider a cyclorotor with 2 hydrofoils, each with a pitch angle of  $\phi = 0^\circ$ .  
 429 The rotor has a radius  $R = 6$  m and a submergence of  $y_0 = -10$  m. For this analysis, we consider a sea state with  
 430 the highest probability of occurrence shown in Figure 9, i.e.  $T_p = 8$  s and  $H_s = 2$  m. The chord length of the foils is  
 431  $C = 6$  m.

432 For the monochromatic sea state test, we evaluate the influence of the spring stiffness  $\kappa$  on the changes of the  
 433 angle of attack  $\alpha$ , within a wave period  $T$ . We test three different spring stiffnesses  $\kappa = 1000$  MN/m,  $\kappa = 1$  MN/m,  
 434 and  $\kappa = 0.1$  MN/m to represent rigid, intermediate and flexible stiffness, respectively. The corresponding changes  
 435 of the angle of attack in one of the hydrofoils of the cyclorotor are presented in Figure 17. It can be seen that peak  
 436 loading alleviation occurs with intermediate and low stiffness. However, the mean angle of attack decreases with lower  
 437 stiffness. This means that the amplitude of both  $F_R$  and  $F_T$  will also decrease. Considering these results, a reduction  
 438 in  $F_R$  is desirable in terms of fatigue damage; however, a reduction in  $F_T$  is detrimental in terms of power output.

439 As part of the regular sea state analysis, we also quantify the change in radial loading for the tested hydrofoil ( $F_R$ )  
 440 and the change in power output ( $J$ ). Assuming a time step of 0.2 s, the high stiffness case  $\kappa = 1000$  MN/m, i.e. the rigid  
 441 foil, yields  $J = 13.2$  kW/s, but a peak radial load of  $F_R = 48.9$  kN. The medium stiffness case  $\kappa = 1$  MN/m, yields  
 442 less energy, with  $J = 11.7$  kW/s, but reduces structural loading, with a peak load of  $F_R = 41.2$  kN. In the low stiffness  
 443 case, where  $\kappa = 0.1$  MN/m, both power production and peak radial loading drop significantly to  $J = 4.6$  kW/s and  
 444  $F_R = 1.8$  kN, respectively.

445 The trends in generated power and maximal tangential loads, with different spring rigidities, is presented in Figure  
 446 18. In agreement with Figure 17, we also consider the sea state with the highest probability of occurrence, i.e.  $T_p = 8$  s  
 447 and  $H_s = 2$  m. In figure 18, we observe that the lower the stiffness, the lower the power production. This is because, at  
 448 the starting equilibrium position, the chord line of the hydrofoil is tangential to the circumferential path of the cyclorotor.  
 449 As such, any pitching motion of the hydrofoil moves the chordline closer to the direction of  $U$ . If the spring has very  
 450 low stiffness, then  $\alpha$  on the hydrofoil can be nullified, as illustrated in Figure 8. Therefore, the stiffness of the spring,  
 451 and of any material used to manufacture a morphing hydrofoil, should be one that allows load alleviation, but prevents  
 452 a total loss of generated power.

453 Once the performance of the passive pitch model was assessed in a regular sea state scenario, we test the model in  
 454 irregular sea state conditions, for  $J$  and  $D$ . For Case 3 we refer to these as  $J_3$  and  $D_3$ . We utilise simulations of one  
 455 hour, as we did previously for Case 1. Here, results are shown for ratios  $J_3/J'_1$  and  $D_3/D'_1$ , in Figure 19a and Figure

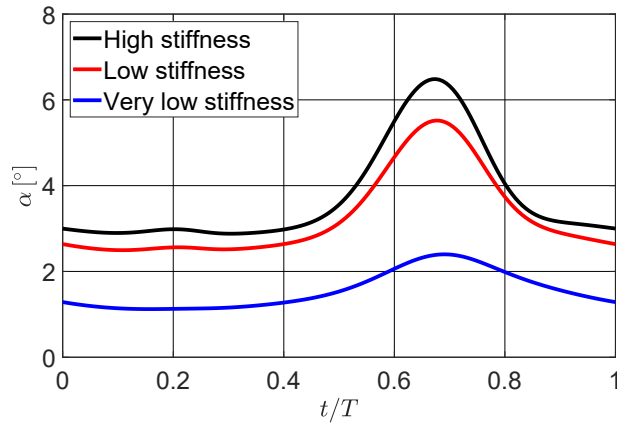


**Figure 17:** Changes in angle of attack for one cycle of rotation  $t/T$ , computed with  $\kappa = 1000, 1$  and  $0.1 \text{ MN/m}$  in black, red, and blue, respectively. Results are presented for hydrofoil 1 and assuming  $H = 2 \text{ m}$  and  $T = 8 \text{ s}$  in regular sea state test.

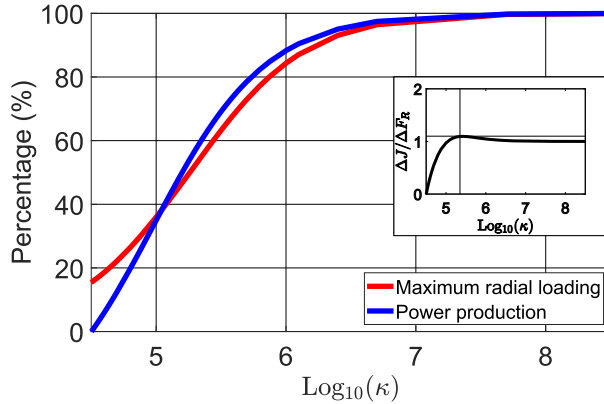


**Figure 18:** Power production and maximal radial loading percentage versus spring rigidity. High rigidity ( $\kappa \geq \text{Log}_{10}(8)$ ) yields 100% of power production and maximal radial loading. Results are computed with  $H = 2 \text{ m}$  and  $T = 8 \text{ s}$  in regular sea state test.

456 19b, respectively. For both foils of the cyclorotor, we select a spring stiffness of  $\kappa = 0.25 \text{ MN/m}$ . This stiffness was  
 457 selected because for the sea state with the highest probability, it provides about 70% of output power and 60% of radial  
 458 force loading with respect to the rigid case, as shown in Figure 18. As such, it is the rigidity that offers the highest  
 459 power to radial loading reduction ratio ( $\Delta J / \Delta F_R$ ), as shown in the inset of Figure 18.

460 Results in Figure 19a show that  $J_3 / J'_1 \geq 0.90$  for most of the tested sea states, with the exception of the upper right  
 461 part of the figure, where  $J_3 / J'_1 < 0.8$ . However, the probability of occurrence of these sea states is much less than  
 462 those where  $J_3 / J'_1 \geq 0.90$ , therefore, the selected spring stiffness shows satisfactory performance in terms of power  
 463 production. In fact, the average loss of power of 10% throughout most of the sea states is significantly smaller than the  
 464 30% power loss that was computed in the regular sea state scenario.

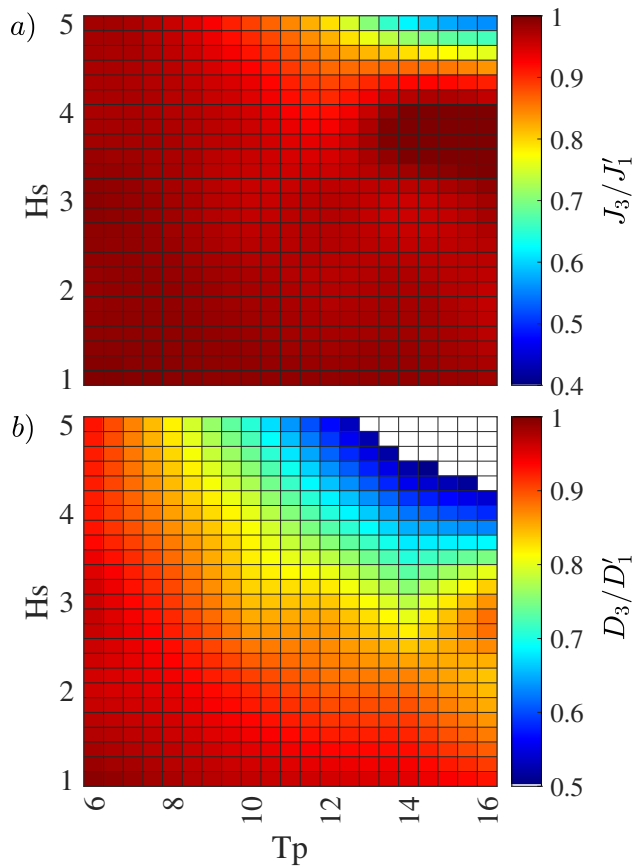


**Figure 19:** a)  $J_3/J'_1$  ratio and b)  $D_3/D'_1$  ratio, with passively pitching foils modelled with the dual spring model.

465 In contrast,  $D_3/D'_1 < 1$  throughout most of Figure 19b. This shows a important reduction in fatigue damage  
 466 compared to that for a rigid hydrofoil case. In particular, the fatigue damage reduction becomes more significant at  
 467 high energy sea states where  $D_3/D'_1 < 0.5$ . These results highlight that a hydrofoil that deforms due the fluid loading  
 468 is useful for wave cycloidal rotors aiming to extend their operational life while incurring a reduced loss in power loss,  
 469 but also a significant reduction in fatigue damage at the hydrofoil stress hot spot.

470 **Case 4: Passively pitching foil with variable rotational velocity**

471 In Case 2, we showed that a variable rotational speed and fixed rigid hydrofoils significantly increase  $J_2/J'_1$ .  
 472 However, this gain comes at the cost of a substantial corresponding increase in  $D_2/D'_1$ . Case 3 shows that passively  
 473 pitching hydrofoils have the potential to reduce  $D_3/D'_1$  at the stress hot spots, although this reduction causes a slight  
 474 drop in power performance. Here, in Case 4, we combine variable rotational velocity control with passively pitching  
 475 foils to test whether this combination can yield an increase in  $J_4/J'_1$ , without a significant penalty in  $D_4/D'_1$ .

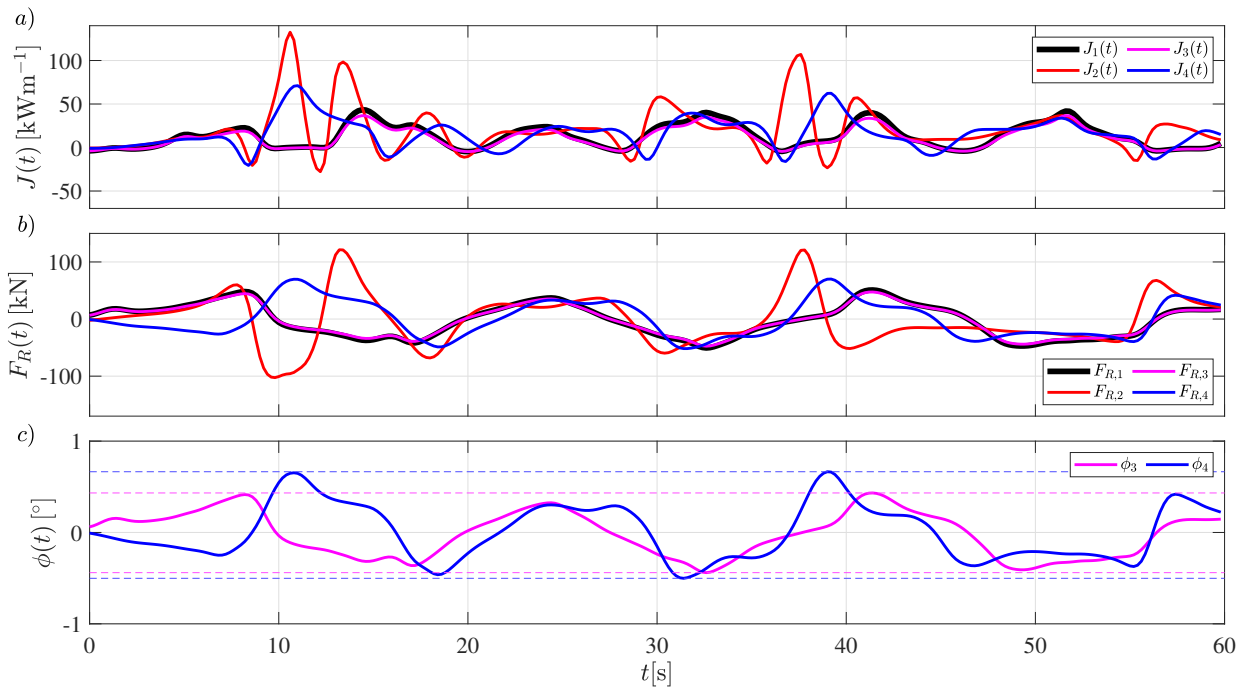


**Figure 20:** Results of simulations for Case 1, 2, 3 and 4 during 60 seconds of high-energy panchromatic wave, with  $T_p=14$  s and  $H_s=4$  m.

476      Because  $F_R$  on the hydrofoils increases due to real-time control of rotational velocity, for this case, we tune the  
 477      stiffness of the spring in the passively pitching model, by testing the performance of the system in a high energy sea  
 478      state. As such, we first simulate  $J(t)$ ,  $F_R(t)$  and  $\phi(t)$  for 60 seconds of simulation in extreme waves, i.e.  $T_p=14$  s and  
 479       $H_s=4$  m.

480      We compare the results of Case 4 to those of Cases 1, 2 and 3 in Figure 20. The figure shows the instantaneous  
 481       $J$  and instantaneous  $F_R$ , for the four tested cases in Figure 20a and Figure 20b, respectively. We refer to the power  
 482      production in each case as  $J_1(t)$ ,  $J_2(t)$ ,  $J_3(t)$  and  $J_4(t)$ , and to the radial forces in one of the foils as  $F_{R,1}(t)$ ,  $F_{R,2}(t)$ ,  
 483       $F_{R,3}(t)$  and  $F_{R,4}(t)$ . Only the forces for one hydrofoil are presented, since the trends observed in  $F_R$  are similar for the  
 484      second hydrofoil.

485      In Figure 20a and Figure 20b, we plot  $J$  and  $F_R$  in black, red, magenta and blue solid lines for Cases 1, 2, 3 and  
 486      4, respectively. In these figures,  $J_1$  and  $F_{R,1}$  are plotted with a thicker line than the other cases, since they represent  
 487      the baseline case. Then, in Figure 20c, we show the instantaneous variation of  $\phi$  for the passively pitching cases (Case  
 488      3 and Case 4) as  $\phi_3$  and  $\phi_4$  in magenta and blue solid lines, respectively. The dotted lines show the maximum and  
 489      minimum values of  $\phi$  for  $\phi_3$  and  $\phi_4$ .

490      The selected stiffness of the spring is  $\kappa = 1.5$  MN/m. This is in the range of medium stiffness tested in Figure 17a  
 491      and about 6 times higher than the stiffness used for the irregular sea states of Case 3. This is because radial loads and

492 fatigue damage increase in these orders of magnitude with respect to constant rotational velocity and rigid hydrofoils,  
 493 as demonstrated in Figure 16b for Case 2.

494 Figure 20a shows that the largest peaks of power occur at  $J_2$ , while  $J_3$  shows a similar behaviour to  $J_1$ , due to the  
 495 rigidity of the spring. It is observed that  $J_4$  corresponds to higher power yield than  $J_1$  and  $J_3$ , but a lower yield than  $J_2$ .  
 496 In fact, in Figure 20a, the average  $J_1$  is 13kW, while  $J_2$  is 20.5kW.  $J_3$  drops to 11.2kW, while  $J_4$  is 16.6kW. This results  
 497 are in line with the analysis of results previously presented in this Section for Case 1, Case 2 and Case 3. By comparison,  
 498 Figure 20b shows that the maximum peaks of  $F_R$  also occur in Case 2, i.e.  $F_{R,2}$ , followed by  $F_{R,4}$ ,  $F_{R,1}$  and  $F_{R,3}$ . In  
 499 terms of maximum values,  $F_{R,2} = 121.0kN$ , while  $F_{R,1} = 53.6kN$ ,  $F_{R,3} = 48.3kN$ , and  $F_{R,4} = 65.8kN$ . The main  
 500 difference between Figures 20a and 20b is that although  $J$  is mostly positive throughout the entire simulation,  $F_R$  does  
 501 experience changes in sign and can exert compression or tension on the support structure of the hydrofoils. This has an  
 502 effect on the pitching motion profile of Cases 3 and 4, as show in Figure 20c. Figure 20c shows the instantaneous  $\phi_3$   
 503 and  $\phi_4$ , for Cases 3 and 4, i.e. the passively pitching cases. We observe that the trends of  $\phi_3$  and  $\phi_4$  follow the trends  
 504 of  $F_{R,3}$  and  $F_{R,4}$ . This is because the sign of  $F_R$  determines the direction of motion of  $\phi$ , as depicted in Figures 7 and  
 505 8. Finally, we recall that the range of motion of  $\phi$  is determined by the stiffness of the torsional spring. We can see  
 506 that, in Figure 20c, although both curves are simulated with the same spring stiffness, the range of motion for Case 3  
 507 is less severe than the one experienced in Case 4, due to the inclusion of variable rotational speed in the latter.

508 Importantly, variable rotational velocity and passively pitching foils require a different torque control solution than  
 509 the case of variable rotational velocity with rigid hydrofoils. Therefore the optimal torque solution for each tested  
 510 sea state needs to be recomputed. As an illustrative example, of how the solution varies between these scenarios, we  
 511 simulate an irregular sea state of 60 seconds of extreme panchromatic waves with  $T_p=14$  s and  $H_s=4$  m. The free  
 512 surface elevation of the simulation is shown, with a blue solid line, in Figure 21. The variable rotational solutions,  
 513 for rigid and passively pitching hydrofoils, are shown in Figure 21, with solid and dotted black lines, respectively. By  
 514 assuming a consistent value of  $\kappa= 1.5$  MN/m, we note that both solutions are different to each other, with the passive  
 515 solution showing smoother transitions between 10 and 25 s, and between 40 and 55 s, with a potential for ease of  
 516 control as well.

517 To complete the analysis for Case 4, we plot the  $J_4/J'_1$  and  $D_4/D'_1$  ratios in Figures 22a and 22b, respectively.  
 518 Similar to Case 2, five simulations with a duration of 60 seconds were run to compute the ratios. Results show that,  
 519 in general  $1 < J_4/J'_1 \leq 2.2$ . Although these results are slightly lower than those for Case 2, they still show capability  
 520 of enhanced power production with respect to the baseline  $J'_1$ . Furthermore, Figure 22b shows that  $D_4/D'_1$  is further  
 521 reduced with respect to  $D_2/D'_1$ . We recall that Case 2 showed that  $10 < D_2/D'_1 < 80$ , while here, in most of the sea  
 522 states,  $1 < D_4/D'_1 < 10$ .

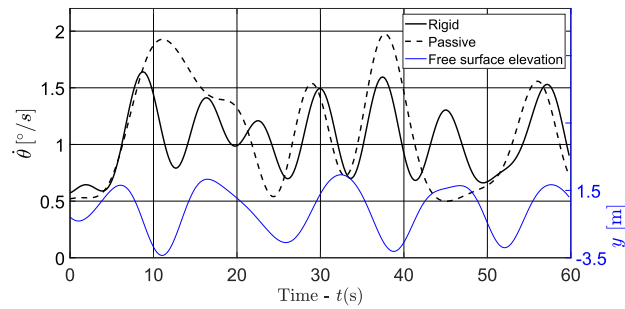


**Figure 21:** Free surface elevation above the rotor centre and optimal variable rotational rate  $\tilde{\omega}$  control solutions, for the cases of rigid and flexible pitches.

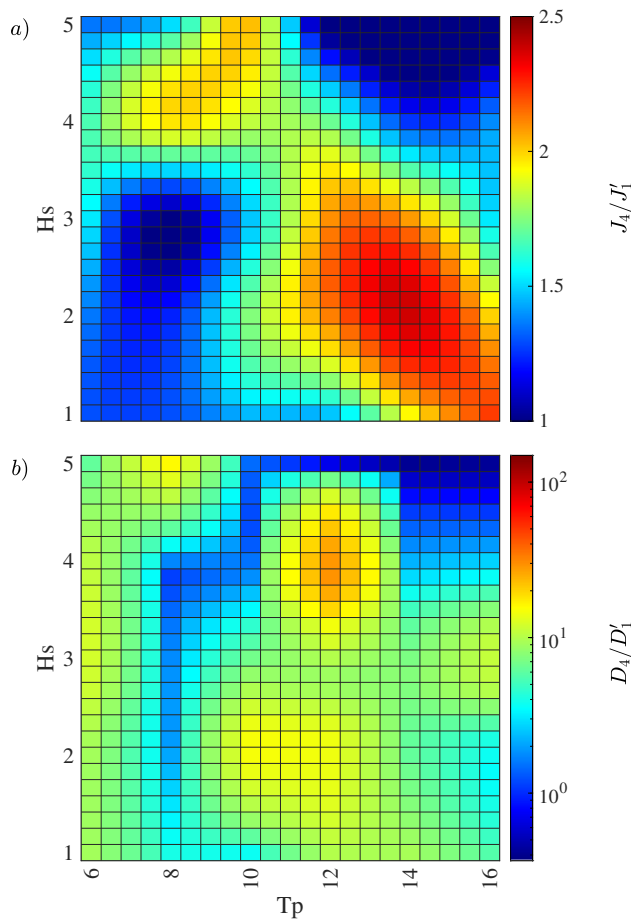


**Figure 22:** a)  $J_4/J_1$  ratio and b)  $D_4/D_1'$  ratio, with variable time dependent rotational velocity and passively pitching foils, modelled with the dual spring model.

#### 523 **Transition map between the four tested cases**

524 In this section, we provide a visual map of the four tested cases, as a function of power and fatigue damage at the  
 525 stress hot spot. The map is shown in Figure 23 and we utilise the map to show the transition paths between cases. We

526 categorise the cases in red, yellow and green, where green is the most desirable and red the less desirable scenario.  
 527 In the figure, the horizontal axis denotes power  $J$ , while the vertical axis denotes fatigue damage  $D$ . The arrows in  
 528 the figure show how we can transition from case to case by incorporating a single step change in control strategy.  
 529 From Case 1, we can transit to Case 2 or Case 3, and from Case 2 or Case 3, we can transit to Case 4. The arrows are  
 530 bidirectional because each control modification is reversible.

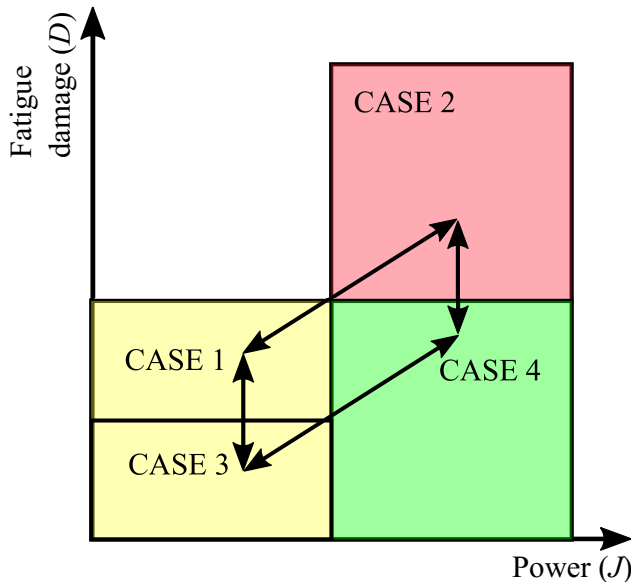


**Figure 23:** Transition color code map between four tested cases showing color coded severity of cases as green-low, yellow-medium and red-high severity.

531 Note that, in (red) Case 2, although the gain in  $J$  is the highest, it also causes the highest  $D$  at the stress hot spots  
 532 and has the highest potential to damage the hydrofoils of the wave cycloidal rotor. In a (yellow) intermediate category,  
 533 both Cases 1 and 3 yield a lower  $D$  than Case 2, but a lower  $J$  as well. Therefore, although these cases are not likely  
 534 to damage the device, they are likely to capture energy less efficiently. Lastly, Case 4 (green) yields a high  $J$  output at  
 535 a low  $D$ . Hence, this is the ideal scenario of operation.

## 536 5. Conclusions

537 In this paper, we present a theoretical/numerical study using different control strategies for a two-foil wave cycloidal  
 538 rotor. Control strategies in a cyclorotor are of particular interest because they have not been extensively explored in  
 539 the literature and because they could be used to enhance power extraction and mitigate fatigue damage. In this paper,  
 540 we study the effect of variable rotational velocity combined with, for the first time, passively pitching hydrofoils, in  
 541 the context of wave cycloidal rotors. We note that the latter is a simplified representation of the behaviour of a  
 542 fully-morphing foil.

543 We assess the impact of variable rotational speed and passively pitching hydrofoils in isolation, and in combination,  
 544 using average power output and the fatigue damage at the hydrofoil stress hot spot, as metrics. In this work, we consider  
 545 a sample stress hot spot located at the fixed end of the hydrofoil, assuming the foil is supported at both ends. The loads  
 546 on the hydrofoils are modelled through a single point vortex model, which has been used to estimate wave generation  
 547 downstream of the rotor and loading on the foils of wave cycloidal rotor [7, 24, 26, 46, 47].

548 Results were analysed for four control strategies. Case 1 is the baseline case, where a constant rotational velocity  
 549 and rigid hydrofoils are used. Case 2 uses a variable rotational velocity with rigid hydrofoils, while Case 3 analyses  
 550 constant rotational velocity with passively pitching hydrofoils. Lastly, Case 4 combines both variable rotational velocity  
 551 and passively pitching hydrofoils.

552 Our study shows that for constant rotational velocity, there is a specific rotational velocity  $\omega$  that maximises power  
 553 extraction for different sea states. This optimal  $\omega$  usually grows with  $T_p$  and  $H_s$ . We also show that the fatigue damage  
 554 distribution is affected by  $H_s$ ,  $T_p$  and  $P_i$ . The larger  $H_s$  is, the larger the loads on the foils and the fatigue damage. The  
 555 shorter  $T_p$  is, the faster the rotor spins, and therefore, the higher the number of fatigue cycles. Lastly, the distribution  
 556 of  $P_i$  shifts the damage peak towards those sea states with the highest probability of occurrence.

557 Variable rotational velocity control shows that, in agreement with the findings of Ermakov et al. [21, 22], there  
 558 is a time dependent rotational velocity solution that increases power extraction. We also show that variable velocity  
 559 increases the fatigue penalty in the hydrofoil stress hot spot by a factor of 10 to 80 times, with respect to the baseline  
 560 case. Therefore, although variable rotational velocity increases power extraction between 50% to 150%, this control  
 561 strategy, on its own is not sustainable for the long term operation of wave cycloidal rotors.

562 In Case 3, we develop a passively pitching model of a hydrofoil, suitable for a wave cycloidal rotor subject to  
 563 irregular waves. The model shows that the passively pitching hydrofoil is effective in mitigating fatigue damage at the  
 564 sample stress hot spot; however, this reduction in fatigue damage is also associated with a drop in power production.  
 565 Therefore in Case 4, we seek to combine variable rotational velocity control with passively pitching hydrofoils to  
 566 increase power production but with a low structural penalty.

567 Finally, Case 4 shows that both a gain in power and a reduction in fatigue damage, are attained. Therefore, we can  
 568 conclude that variable rotational velocity and passively pitching hydrofoils complement each other to enhance both  
 569 power production and the structural performance of the cyclorotor. In conclusion, the possibilities for control for wave  
 570 cycloidal rotors are vast. As such, in this study, we present the first attempt to analyse a few key possible configurations,  
 571 with the use of high performance computations. Our results show promise to increase both power extraction and at the  
 572 same time, reduce fatigue damage of the device.

573 **Acknowledgement**

574 Results were obtained using the Irish Centre for High-End Computing (ICHEC) (<https://www.ichec.ie/>) and the  
575 ARCHIE-WeSt High Performance Computer ([www.archie-west.ac.uk](http://www.archie-west.ac.uk)) based at the University of Strathclyde.

576 **CRediT authorship contribution statement**

577 **Abel Arredondo-Galeana:** Writing - original draft, Conceptualization, Methodology, Formal analysis, Investigation,  
578 Data processing.. **Andrei Ermakov:** Writing - original draft, Conceptualization, Methodology, Formal analysis,  
579 Investigation, Data processing.. **Weichao Shi:** Writing - review and editing, Conceptualization, Supervision, Funding  
580 acquisition.. **John V. Ringwood:** Writing - review and editing, Conceptualization, Supervision, Funding acquisition..  
581 **Feargal Brennan:** Writing - review and editing, Conceptualization, Supervision, Funding acquisition..

582 **References**

- 583 [1] Abbot, I.H., Doenhoff, A.E., 1959. Theory of wing sections: including a summary of airfoil data. first ed.. Dover Publications, Inc.
- 584 [2] Accensi, M., Maisondieu, C., 2015. HOMERE. Ifremer - Laboratoire Comportement des Structures en Mer. doi:<https://doi.org/10.12770/cf47e08d-1455-4254-955e-d66225c9dc90>.
- 585 [3] Ahn, S., 2021. Modeling mean relation between peak period and energy period of ocean surface wave systems. Ocean Engineering 228, 108937.
- 586 [4] Airy, G.B., 1985. Tides and waves. 192, Encyc. Metro.
- 587 [5] Arredondo-Galeana, A., Brennan, F., 2021. Floating offshore vertical axis wind turbines: Opportunities, challenges and way forward. Energies 14. URL: <https://www.mdpi.com/1996-1073/14/23/8000>, doi:10.3390/en14238000.
- 588 [6] Arredondo-Galeana, A., Olbert, G., Shi, W., Brennan, F., . Near wake hydrodynamics and structural design of a single foil cycloidal rotor in regular waves. Available at SSRN: <https://ssrn.com/abstract=4239352>.
- 589 [7] Arredondo-Galeana, A., Shi, W., Olbert, G., Scharf, M., Ermakov, A., Ringwood, J., Brennan, F., 2021a. A methodology for the structural design of LiftWEC: A wave-bladed cyclorotor, in: Proceedings of the 14th European Wave and Tidal Energy Conference, Plymouth, UK.
- 590 [8] Arredondo-Galeana, A., Young, A.M., Smyth, A.S., Viola, I.M., 2021b. Unsteady load mitigation through a passive trailing-edge flap. Journal of Fluids and Structures 106, 103352. URL: <https://www.sciencedirect.com/science/article/pii/S0889974621001353>, doi:<https://doi.org/10.1016/j.jfluidstructs.2021.103352>.
- 591 [9] Atargis, the Energy Corporation, 2021. Available: <https://atargis.com/> [Accessed: 22-May-2022].
- 592 [10] Bacelli, G., Spencer, S.J., Patterson, D.C., Coe, R.G., 2019. Wave tank and bench-top control testing of a wave energy converter. Applied Ocean Research 86, 351–366.
- 593 [11] Bai, X., Zhao, Y., Dong, G., Bi, C., 2018. Probabilistic analysis and fatigue life assessment of floating collar of fish cage due to random wave loads. Applied Ocean Research 81, 93–105. doi:<https://doi.org/10.1016/j.apor.2018.09.018>.
- 594 [12] Burton, T., N., J., Sharpe, 2011. Wind Energy Handbook. second ed.. Wiley.
- 595 [13] Cao, Y., Liu, A., Yu, X., Liu, Z., Tang, X., Wang, S., 2021. Experimental tests and cfd simulations of a horizontal wave flow turbine under the joint waves and currents. Ocean Engineering 237, 109480. doi:<https://doi.org/10.1016/j.oceaneng.2021.109480>.

- 606 [14] Cheng, Y., Fu, L., Dai, S., Collu, M., Cui, L., Yuan, Z., Incecik, A., 2022. Experimental and numerical analysis of a hybrid wec-  
 607 breakwater system combining an oscillating water column and an oscillating buoy. *Renewable and Sustainable Energy Reviews* 169,  
 608 112909. URL: <https://www.sciencedirect.com/science/article/pii/S1364032122007900>, doi:<https://doi.org/10.1016/j.rser.2022.112909>.
- 610 [15] Cornett, A.M., 2008. *A Global Wave Energy Resource Assessment*.
- 611 [16] Cummins, C.P., Scarlett, G.T., Windt, C., 2022. Numerical analysis of wave–structure interaction of regular waves with surface-piercing  
 612 inclined plates. *Journal of Ocean Engineering and Marine Energy* 8, 99–115. URL: <https://doi.org/10.1007/s40722-021-00219-6>,  
 613 doi:[10.1007/s40722-021-00219-6](https://doi.org/10.1007/s40722-021-00219-6).
- 614 [17] Dai, W., Broglia, R., Viola, I.M., 2022. Mitigation of rotor thrust fluctuations through passive pitch. *Journal of Fluids and Structures* 112,  
 615 103599. URL: <https://www.sciencedirect.com/science/article/pii/S0889974622000573>, doi:<https://doi.org/10.1016/j.jfluidstructs.2022.103599>.
- 617 [18] DNV, 2007. Recommended Practice DNV-RP-C205. Environmental conditions and environmental loads. Det Norske Veritas, Høvik, Norway.
- 618 [19] DNV, 2011. Recommended Practice DNV-RP-C203. Fatigue Design of Offshore Steel Structures. Det Norske Veritas, Høvik, Norway.
- 619 [20] Durand, M., Babarit, A., Pettinotti, B., Quillard, O., Toulaastel, J., Clément, A., 2007. Experimental validation of the performances of the  
 620 searev wave energy converter with real time latching control, in: Proc. of the 7th Euro. Wave and Todal Energy Conf., Porto.
- 621 [21] Ermakov, A., Marie, A., Ringwood, J.V., 2022a. Optimal control of pitch and rotational velocity for a cyclorotor wave energy device. *IEEE*  
 622 Transactions on Sustainable Energy 13, 1631–1640.
- 623 [22] Ermakov, A., Marie, A., Ringwood, J.V., 2022b. Some fundamental results for cyclorotor wave energy converters for optimum power capture.  
 624 *IEEE Transactions on Sustainable Energy* 13, 1869–1872.
- 625 [23] Ermakov, A., Ringwood, J.V., 2021a. A control-orientated analytical model for a cyclorotor wave energy device with n hydrofoils. *Journal of*  
 626 *Ocean Engineering and Marine Energy* 7, 201–210.
- 627 [24] Ermakov, A., Ringwood, J.V., 2021b. Development of an analytical model for a cyclorotor wave energy device, in: Proceedings of 14th  
 628 European Wave and Tidal Energy Conference, paper #1885, Plymouth, UK.
- 629 [25] Ermakov, A., Ringwood, J.V., 2021c. Rotors for wave energy conversion—practice and possibilities. *IET Renewable Power Generation* 15,  
 630 3091–3108. doi:[10.1049/rpg2.12192](https://doi.org/10.1049/rpg2.12192).
- 631 [26] Ermakov, A., Ringwood, J.V., 2022. A validated analytical model for a cyclorotor wave energy device. *International Marine Energy Journal*  
 632 5, 201–208.
- 633 [27] Ermakov, A.M., Ringwood, J.V., 2021d. Erratum to: A control-orientated analytical model for a cyclorotor wave energy device with n  
 634 hydrofoils. *Journal of Ocean Engineering and Marine Energy* 7, 493–494.
- 635 [28] Fernández-Chozas, J., Tetu, A., Arredondo-Galeana, A., 2021. Parametric cost model for the initial techno-economic assessment of lift-force  
 636 based wave energy converters, in: Proceedings of the 14th European Wave and Tidal Energy Conference.
- 637 [29] García-Violini, D., Peña-Sánchez, Y., Faedo, N., Windt, C., Ferri, F., Ringwood, J.V., 2021. Experimental implementation and validation of a  
 638 broadband lti energy-maximizing control strategy for the wavestar device. *IEEE Transactions on Control Systems Technology* 29, 2609–2621.
- 639 [30] Hermans, A., Van Sabben, E., Pinkster, J., 1990. A device to extract energy from water waves. *Applied Ocean Research* 12, 175 – 179.  
 640 doi:[https://doi.org/10.1016/S0141-1187\(05\)80024-0](https://doi.org/10.1016/S0141-1187(05)80024-0).
- 641 [31] Hoerner, S., Abbaszadeh, S., Cleynen, O., Bonamy, C., Maître, T., Thévenin, D., 2021. Passive flow control mechanisms with bioinspired  
 642 flexible blades in cross-flow tidal turbines. *Experiments in Fluids* 62, 104. doi:[10.1007/s00348-021-03186-8](https://doi.org/10.1007/s00348-021-03186-8).

- 643 [32] Hoerner, S., Abbaszadeh, S., Maître, T., Cleynen, O., Thévenin, D., 2019. Characteristics of the fluid–structure interaction within darrieus  
 644 water turbines with highly flexible blades. *Journal of Fluids and Structures* 88, 13–30. URL: <https://www.sciencedirect.com/science/article/pii/S0889974618309861>, doi:<https://doi.org/10.1016/j.jfluidstructs.2019.04.011>.
- 645 [33] Jalón, M.L., Brennan, F., 2020. Hydrodynamic efficiency versus structural longevity of a fixed owc wave energy converter. *Ocean Engineering*  
 646 206, 107260. doi:<https://doi.org/10.1016/j.oceaneng.2020.107260>.
- 647 [34] Jeans, T., Fagley, C., Siegel, S., Seidel, J., 2013. Irregular deep ocean wave energy attenuation using a cycloidal wave energy converter.  
 648 *International Journal of Marine Energy* 1, 16 – 32. doi:<https://doi.org/10.1016/j.ijome.2013.06.001>.
- 649 [35] Kong, F., Su, W., Liu, H., Collu, M., Lin, Z., Chen, H., Zheng, X., 2019. Investigation on pto control of a combined axisymmetric buoy-wec(cab-  
 650 wec). *Ocean Engineering* 188, 106245. URL: <https://www.sciencedirect.com/science/article/pii/S0029801819304238>,  
 651 doi:<https://doi.org/10.1016/j.oceaneng.2019.106245>.
- 652 [36] Lamont-Kane, P., Folley, M., Frost, C., Whittaker, T., 2021. Preliminary Investigations into the Hydrodynamic Performance of Lift-Based  
 653 Wave Energy Converters.
- 654 [37] LiftWEC Consortium, 2021. Available: <https://liftwec.com/> [Accessed: 17-May-2022].
- 655 [38] McCormick, M., 2013. Ocean wave energy conversion. Dover edition ed., Dover Publications Inc.
- 656 [39] Mérigaud, A., Ringwood, J.V., 2018. Free-surface time-series generation for wave energy applications. *IEEE Journal of Oceanic Engineering*  
 657 43, 19–35.
- 658 [40] Mohtat, A., Fagley, C., Chitale, K.C., Siegel, S.G., 2022. Efficiency analysis of the cycloidal wave energy convertor under real-time dynamic  
 659 control using a 3d radiation model. *International Marine Energy Journal* 5, 45–56.
- 660 [41] Pisetta, G., Le Mestre, R., Viola, I.M., 2022. Morphing blades for tidal turbines: A theoretical study. *Renewable Energy* 183, 802–  
 661 819. URL: <https://www.sciencedirect.com/science/article/pii/S0960148121015433>, doi:<https://doi.org/10.1016/j.renene.2021.10.085>.
- 662 [42] Press, W., Teukolsky, S., Vetterling, W., Flannery, B., 2007. Numerical recipes : the art of scientific computing. 3rd ed.. ed., Cambridge  
 663 University Press, New York.
- 664 [43] Ringwood, J.V., 2020. Wave energy control: status and perspectives 2020. *IFAC-PapersOnLine* 53, 12271–12282.
- 665 [44] Ringwood, J.V., Bacelli, G., Fusco, F., 2014. Energy-maximizing control of wave-energy converters: The development of control system  
 666 technology to optimize their operation. *IEEE Control Systems Magazine* 34, 30–55. doi:[10.1109/MCS.2014.2333253](https://doi.org/10.1109/MCS.2014.2333253).
- 667 [45] Ringwood, J.V., Ermakov, A., 2022. Energy-maximising control philosophy for a cyclorotor wave energy device, in: 41st International  
 668 Conference on Ocean, Offshore & Arctic Engineering (OMAE), Hamburg, American Society of Mechanical Engineers.
- 669 [46] Siegel, S., Jeans, T., McLaughlin, T., 2011. Deep ocean wave energy conversion using a cycloidal turbine. *Applied Ocean Research* 33, 110  
 670 – 119. doi:<https://doi.org/10.1016/j.apor.2011.01.004>.
- 671 [47] Siegel, S.G., 2019. Numerical benchmarking study of a cycloidal wave energy converter. *Renewable Energy* 134, 390 – 405. doi:<https://doi.org/10.1016/j.renene.2018.11.041>.
- 672 [48] Stansby, P., Carpintero Moreno, E., Stallard, T., 2017. Large capacity multi-float configurations for the wave energy converter m4 using a  
 673 time-domain linear diffraction model. *Applied Ocean Research* 68, 53–64. URL: <https://www.sciencedirect.com/science/article/pii/S0141118717302146>, doi:<https://doi.org/10.1016/j.apor.2017.07.018>.
- 674 [49] Viola, I.M., Pisetta, G., Dai, W., Arredondo-Galeana, A., Young, A.M., Smyth, A.S., 2022. Morphing blades: Theory and proof of principles.  
 675 International Marine Energy Journal .

- 680 [50] Wehausen, J.V., Laitone, E.V., 1960. Surface Waves. Springer Berlin Heidelberg, Berlin, Heidelberg. pp. 446–778. doi:10.1007/  
681 978-3-642-45944-3\_6.
- 682 [51] Whittaker, T., Folley, M., 2012. Nearshore oscillating wave surge converters and the development of oyster. Philosophical Transactions of the  
683 Royal Society A: Mathematical, Physical and Engineering Sciences 370, 345–364. doi:10.1098/rsta.2011.0152.
- 684 [52] Wu, X., Zuo, L., 2022. Preliminary modeling of angle of attack in self-rectifying turbine under high rotational speed, in: Proceedings of the  
685 ASME: the 34th Conference on Mechanical Vibration and Sound (VIB).
- 686 [53] Yang, L., Huang, J., Congpuong, N., Chen, S., Mi, J., Bacelli, G., Zuo, L., 2021. Control co-design and characterization of a power  
687 takeoff for wave energy conversion based on active mechanical motion rectification. IFAC-PapersOnLine 54, 198–203. doi:<https://doi.org/10.1016/j.ifacol.2021.11.175>. modeling, Estimation and Control Conference MECC 2021.
- 688 [54] Zang, Z., Zhang, Q., Qi, Y., Fu, X., 2018. Hydrodynamic responses and efficiency analyses of a heaving-buoy wave energy converter with pto  
689 damping in regular and irregular waves. Renewable Energy 116, 527–542. URL: <https://www.sciencedirect.com/science/article/pii/S0960148117309199>, doi:<https://doi.org/10.1016/j.renene.2017.09.057>.
- 692 Dr Abel Arredondo-Gaelana is a Postdoctoral Research Associate at the Department of Naval, Marine and Ocean Engineering at the University of  
693 Strathclyde.
- 694 Dr Andrei Ermakov is a Postdoctoral Researcher at the Centre for Ocean Energy Research, Maynooth University, Ireland.
- 695 Dr Weichao Shi is Senior Lecturer at the Department of Naval, Marine and Ocean Engineering at the University of Strathclyde.
- 696 Prof John V. Ringwood is the Director of the Centre for Ocean Energy Research, Maynooth University, Ireland.
- 697 Prof Feargal Brennan is Head of the Department of Naval, Marine and Ocean Engineering at the University of Strathclyde.

## Nomenclature

$a$	Fourier series coefficient [-]	$n_i$	number of cycles in stress block $i$ [-]
$\bar{a}$	intercept of vertical axis of SN curve [-]	$N_i$	number of cycles to failure at stress range $\Delta\sigma$ [-]
$A$	wave amplitude [m]	$P_i$	the probability of the $i$ -th sea
$b$	Fourier series coefficient [-]	$R$	radius of cyclorotor [m]
$c$	Fourier series coefficient [-]	$S$	span of cyclorotors shaft [m]
$C$	hydrofoil chord length [m]	$S_A(\omega_j)$	amplitude of the spectrum at the $j$ -th frequency
$C_0$	distance from pitching axis to quarter chord [m]	$S_{PM}$	Pierson-Moskowitz spectrum
$C_D$	drag coefficient [-]	SHS	square hollow section
$C_L$	lift coefficient [-]	$t$	time [s]
$C_M$	moment coefficient [-]	$T$	monochromatic wave period [s]
$C_{M,1/4}$	quarter chord moment coefficient [-]	$T_0$	the time interval for power calculation [s]
$C_P$	distance from pitching edge to pitching axis [m]	$T_e$	panchromatic wave energy period [s]
$d$	Fourier series coefficient [-]	$T_{ext}$	time interval for energy calculation [s]
$D$	accumulated fatigue damage [-]	$T_p$	panchromatic wave peak period [s]
$D_1$	damage accumulated for rotation with the optimal constant velocity and rigid pitch [-]	$\mathbf{u}$	rotational velocity of the foil [m/s]
$D_2$	damage accumulated for rotation with the optimal variable velocity and rigid pitch [-]	$\mathbf{U}$	relative foil/fluid velocity [m/s]
$D_3$	damage accumulated for rotation with the optimal constant velocity and flexible pitch [-]	$\bar{\mathbf{U}}$	mean inflow velocity [m/s]
$D_4$	damage accumulated for rotation with the optimal variable velocity and flexible pitch [-]	$\mathbf{w}$	wave induced fluid velocity [m/s]
$D_w$	Dawson function	$\mathbf{w}_\Gamma$	foil induced fluid velocity [m/s]
$F(z, t)$	the complex potential for the point vortex [N]	$x$	stream-wise coordinate in the $z$ -plane [m]
$F_L$	lift force [N]	$y$	normal coordinate from the mean water level [m]
$F_D$	drag force [N]	$y_0$	submergence of rotor [m]
$F_T$	tangential force [N]	$y_{xx}$	distance from symmetric horizontal axis to outer shell of the square hollow section [m]
$F_R$	radial force [N]	$z$	complex coordinate
$g$	gravity constant [ $\text{m}^2/\text{s}$ ]	$\alpha$	angle of attack [°]
$h$	total number of harmonics []	$\bar{\alpha}$	non-zero mean angle of attack [°]
$H$	monochromatic wave height [m]	$\beta$	inflow angle of $U$ [°]
$H_s$	significant wave height [m]	$\gamma$	JONSWAP spectrum factor [-]
$I$	Inertia of rotor [ $\text{kg m}^2$ ]	$\Gamma$	instantaneous circulation of point vortex [ $\text{m}^2/\text{s}$ ]
$I_{xx}$	second moment of are of square hollow section [ $\text{m}^4$ ]	$\zeta$	position of point vortex in the $z$ -plane
$J$	mechanical power per second per span meter [ $\text{W s}^{-1} \text{m}^{-1}$ ]	$\zeta'$	position of the mirror point vortex in the $z$ -plane
$J_0$	power generated for rotation with the wave frequency [ $\text{W s}^{-1} \text{m}^{-1}$ ]	$\eta$	wave phase
$J_1$	power generated for rotation with the optimal constant velocity and rigid pitch [ $\text{W s}^{-1} \text{m}^{-1}$ ]	$\theta$	azimuthal position of rotor [°]
$J_2$	power generated for rotation with the optimal variable velocity and rigid pitch [ $\text{W s}^{-1} \text{m}^{-1}$ ]	$\dot{\theta}$	rotational frequency or rate of rotor [°/s]
$J_3$	power generated for rotation with the optimal constant velocity and flexible pitch [ $\text{W s}^{-1} \text{m}^{-1}$ ]	$\ddot{\theta}_0$	optimal rotational frequency or rate of rotor [°/s]
$J_4$	power generated for rotation with the optimal variable velocity and flexible pitch [ $\text{W s}^{-1} \text{m}^{-1}$ ]	$\ddot{\theta}$	rotational acceleration of rotor [°/s <sup>2</sup> ]
$J_w$	power available in irregular waves [ $\text{W s}^{-1} \text{m}^{-1}$ ]	$\kappa$	spring stiffness [N/m]
$k$	wave number [-]	$\lambda$	proportionality coefficient between wave peak and energy periods [-]
$m$	mass of hydrofoil segment [kg]	$\rho$	fluid density [ $\text{kg/m}^3$ ]
$\bar{m}$	negative slope of the SN curve [-]	$\sigma$	parameter of JONSWAP spectrum [-]
$M_0$	torsional moment [Nm]	$\bar{\sigma}$	structural stress [MPa]
$M$	bending moment at stress hot spot of the foil [Nm]	$\tau$	time parameter [s]
$M_H$	hydrodynamic moment [Nm]	$\mathcal{T}_{PTO}$	power take-off torque [Nm]
$\bar{M}_H$	mean hydrodynamic moment [Nm]	$\mathcal{T}_{Wave}$	hydrodynamic torque [Nm]
$M_P$	torsional moment of spring [Nm]	$\phi$	torsional spring deformation or pitch angle displacement [°]
		$\psi$	the initial angular position of each hydrofoil [°]
		$\omega$	wave frequency [°/s]
		$\omega_p$	peak wave frequency [°/s]